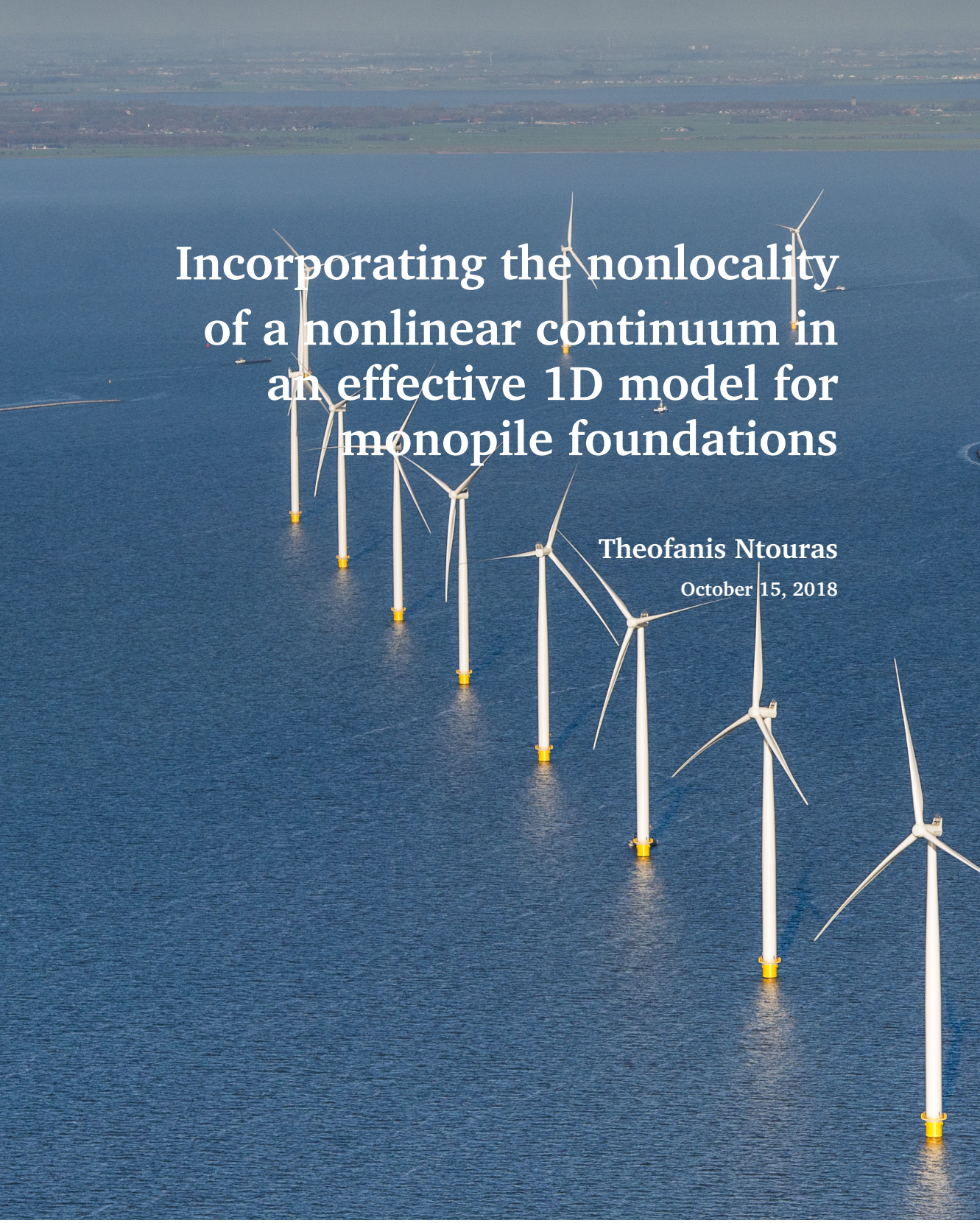

Incorporating the nonlocality of a nonlinear continuum in an effective 1D model for monopile foundations

Theofanis Ntouras

October 15, 2018

TU Delft Delft University of Technology

SIEMENS Gamesa RENEWABLE ENERGY

Incorporating the nonlocality of a nonlinear continuum in an effective 1D model for monopile foundations

Master of Science Thesis

Author:	Theofanis Ntouras	
Committee:	Prof. Dr. A. Metrikine	TU Delft - Chairman
	Ir. J.S Hoving	TU Delft
	Dr.Ir. F. Pisanò	TU Delft
	Dr.Ir. K.N. van Dalen	TU Delft
	Dr.Ir. W.G. Versteijlen	Siemens Gamesa Renewable Energy

October 15, 2018

TU Delft Delft University of Technology

- CONFIDENTIAL -

SIEMENS Gamesa RENEWABLE ENERGY

Summary

World energy consumption rises every year. Therefore, producing renewable and sustainable energy is necessary to protect the viability of this planet. The most well-known and promising form of renewable energy is that of wind power. The limited space in terrestrial areas yielded motivation to the growth of offshore wind industry. Offshore wind turbines (OWT) are most often founded on large-diameter monopiles (MP). Despite of the significant amount of units installed, their design engages Soil Structure Interaction (SSI) models based on slender pile response. The current research focuses on developing a nonlinear nonlocal 1D effective model able to predict the nonlinear response of such a foundation under static loading, incorporating their rigid behavior. This is considered a first step so as advanced nonlinear SSI is incorporated in the design of monopile foundations.

The 1D model is based on Timoshenko beam theory, assuming the beam (representing the MP) is founded on a distributed, Winkler-type foundation, consisting of two types of fully coupled springs, lateral and rotational. These springs allow the model to capture the 3D continuum reaction of the soil towards rigid behaving monopiles.

This type of behavior mobilizes a large volume of the continuum. The term nonlocality describes this global soil response towards the pile. In a nutshell, perturbations in a 3D Finite Element (FE) continuum are performed to capture the global reaction.

The soil profile considered in this study is homogeneous sand. In the Finite Element model it is modeled with a nonlinear constitutive model. This means that a nonlinear relation between the loading on the monopile and the respective displacement exists. The resulting nonlinear response should be captured in the 1D effective model. This is achieved by calculating the stiffness terms of the 1D model for more than one loading combinations on the MP. The obtained nonlocal stiffness matrices contain a 3^{rd} dimension along which the nonlinear soil response is captured. The nonlinear nonlocal stiffness matrices are directly applied in the 1D effective model.

To visualize the performance of the developed model, a comparison between horizontal force - head displacement and overturning moment - head rotation curves calculated by 3D Finite Element Analysis and computed by the 1D effective model is made. The comparison is promising for the examined cases. However, there are still

steps to be taken in order to further validate the method and expand its applicability.

Preface

This project is the last piece of the puzzle called Master of Science. I would like to express my gratefulness to everyone who supported and encouraged me over these two years and especially those who contributed in this thesis.

To begin with, my committee deserves my wholehearted gratitude for the guidance and support it provided. Pim, thank you for giving me the opportunity to "interact" with such a challenging and interesting topic, for the hours you spent mentoring and supervising me and for your patience and your useful comments when reviewing my work. But, most importantly thank you for pointing me the light at the end of the tunnel when I could not see it. Federico, your contribution was invaluable. Any time I needed your opinion and your advice you were there to guide my thoughts to the correct path. Your in depth soil and FEM knowledge in combination with your continuous interest truly helped and inspired me not only in theoretical but also in practical challenges. Karel, thank you for the precious time you dedicated to my work. Jeroen, I honestly appreciate your positive attitude, willing to supplement my committee even on such a short notice. Lastly, Andrei thank you for your overall supervision and your applicable, suitable and appropriate guidance during our meetings.

Nothing would be the same without the friendly and supportive environment I was working in. For that I would like to express my gratitude to all my colleagues at Siemens Gamesa, who added a happy and cheerful note in the graduation process. The table football games are a really refreshing activity that I had the pleasure to share with most of you. Thank you for that. Special thanks to the other students at the office who were a continuous assistant when challenges, in whatever topic, were rising.

Some colleagues though, on top of being welcoming, had also the motivation to instruct me and I highly appreciate it. Sebastiaan, thank you for all the fruitful conversations we had, your time spent reading my "gibberish" and I apologize for not going to pile head deflection of 2 m. Axel, listening to your opinion has only been beneficial to me. Matteo, something did not go that "terribly wrong" in the end. I hope you all enjoyed our "interaction" as much as I did.

Sincere thankfulness to the friends who I met in this two years adventure and unconditionally supported me. Thank you for making my life in the Netherlands

sunnier than it usually is. Greater appreciation to the ones who managed the same from distance. The greatest though is shown to my family. Mom and dad thanks for giving me this opportunity to broaden my horizons.

Theofanis Ntouras
Delft, October 2018

Contents

Nomenclature

Latin symbols

$\bar{\boldsymbol{U}}$	Auxiliary displacement matrix	m^2
$\boldsymbol{F_x}$	Lateral reaction force matrix	N
$\boldsymbol{K_{l,l}}$	Lateral-lateral stiffness matrix	N/m^3
$\boldsymbol{K_{l,r}}$	Lateral-rotational stiffness matrix	N/m^2
$\boldsymbol{K_{r,l}}$	Rotational-lateral stiffness matrix	Nm/m^3
$\boldsymbol{K_{r,r}}$	Rotational-rotational stiffness matrix	Nm/m^2
$\boldsymbol{M_y}$	Overturning reaction moment matrix	Nm
$\boldsymbol{U}$	Matrix of displacements after imposing perturbations	m
A	Cross sectional area	m^2
D	Pile diameter	m
E	Young's Modulus	MPa
F	Horizontal force	N
G	Shear modulus	GPa
h	Vertical discretization height	m
I	Second moment of area	m^4
K_r	Pile flexibility factor	-
L	Pile length	m
M	Overturning moment	Nm
m	Number of nodes on a pile ring	-
n	Ratio of pile length over discretization height	-
u	Lateral pile displacement	m
u'	Lateral pile slope	-

Greek symbols

$\bar{\boldsymbol{\Psi}}$	Auxiliary rotational matrix	m^2
$\boldsymbol{\Psi}$	Matrix of rotation after imposing perturbations	m

δ	Skin friction angle	$^\circ$
κ	Timoshenko Shearing Coefficient	-
ϕ	Internal friction angle	$^\circ$
ψ	Dilatancy angle (Section 3.1)	$^\circ$
ψ	Lateral pile rotation	rad
ψ'	Lateral pile curvature	rad/m^{-1}

Abbreviations

1 & 3D	One & three dimensions respectively
DoF	Degree of Freedom
FD	Finite difference
FEA	Finite element analysis
FEM	Finite element method
LCoE	Levelized cost of energy
MC	Mohr-Coulomb
MP	Monopile
OWT	Offshore wind turbine
RNA	Rotor nacelle assembly
SSI	Soil structure interaction

1
Introduction

This thesis project is motivated by the extensive use of MP foundations in the offshore wind industry. To clarify, the ultimate goal of this research is to develop a nonlinear nonlocal 1D effective model capturing the rigid behavior of a MP foundation and being able to predict its nonlinear response under static loading. This introductory chapter begins with a fast flashback regarding wind energy, followed by the current industry techniques and related studies concerning modeling a MP foundation and the respective Soil Structure Interaction (SSI). Afterwards, the objective of this project is presented and finally the layout of the text is introduced.

1.1. General Introduction

World energy consumption rises every year. This trend is predicted to continue with an increase of approximately 30% by 2040 [8]. Therefore, producing renewable and sustainable energy is necessary to secure the viability of our planet. The most well-known and promising form of renewable energy is that of wind power. Mankind has been using the power of wind to its benefit since the 1st century AD [11]. Back then, the wind flow was used to power machines, but in the late 19th century the first windmill for production of electricity was built [21].

The interest in wind energy is climbing since then. Especially in the 21st century the developments of the wind industry were astonishing. Even from the end of the previous century, wind turbines started to be placed in groups forming wind farms. Nowadays, not only because of limited space onshore but also due to smoother and more efficient wind conditions offshore, the wind farms are moving seaward. By 2015 the global wind power generation capacity had reached 7% of the total. However, less than 3% of this production was from offshore wind [9]. Nonetheless, offshore wind industry is flourishing and the challenge of building safe and robust but economically competitive farms is rising.

The most common foundation solution for an offshore wind turbine is a monopile, large-diameter circular steel structures. In contrast with its relative simplicity and the significant amount of units being installed, there is still room for improvement in the design that could decrease the Levelized Cost of Energy (LCoE) [19]. This efficient design of laterally loaded monopiles is the fundamental motivation of this thesis project.

1.2. Current industry practice and related studies

Wind industry established in the offshore environment long after the oil & gas industry. Therefore, the former based on techniques and experience gained by the latter. Thus, offshore wind industry has adopted the *p-y* curve approach for modeling the SSI of a laterally loaded MP foundation. This approach is a semi-empirical method which connects the pile displacement y, at specific depths, with the local soil resistance p. The tangent of such a curve, derivative of resistance with respect to displacement, is used in a Euler-Bernulli Beam-on-Winkler foundation model (nonlinear elastic springs), developed for both sandy [22, 18] and clayey soils[17].

However, these models have been calibrated with field tests on slender piles and the contained soil reaction mechanisms are limited to those developed on slender piles (local due to bending of the pile). In contrast, the size of MP foundation is growing and the response can not be called flexible. A larger part of the continuum is mobilized to react on the rigid behavior, meaning the response is more global (nonlocal) [5]. Therefore, extra reaction mechanisms are introduced. Vertical shearing on the pile wall creates distributed moments along the depth. Moreover, at the tip of the pile due to the rigid "toe kick" a lateral force and moment are introduced [12, 13]. Neither the last mechanisms nor the nonlocality can be captured with a model including only uncoupled lateral springs as the *p-y* method proposes.

These concerns regarding the *p-y* approach have raised motivation for extensive work on the subject of modeling SSI for laterally loaded large diameter piles. Notable was the work of Byrne et al. [7], who developed a 1D FE model based on the conventional *p-y* approach. More specifically, it was proposed to model the MP as a beam based on Timoshenko theory. Moreover, all the aforementioned soil reaction mechanisms are incorporated. To clarify, it is assumed that distributed lateral force and moment are acting along the embedded length of the pile. The latter is presumed to be highly important in Ultimate Limit State (ULS) loading, due to the expected wedge-type failure mechanism of rigidly behaving piles (in contrast with the flow around mechanism of slender piles). The model also takes into consideration the tip resistance by considering a discrete lateral force and moment acting at the base of the foundation.

All the above-mentioned soil reactions on the pile are represented by reaction curves. These can be extracted from 3D FEA. The benefit of such a process is that the more sophisticated and advanced the 3D modeling is, the better the 1D model. Therefore, there is space for continuous evolution of the method. The research of Byrne et al.[7] was not the first that proposed the use of a 3D model to capture the global soil response mobilized by a rigid behavior of laterally loaded MP ([1, 14, 23] only to mention a few), but it managed to incorporate results of 3D FEA into a simpler and faster 1D FE design model.

The lastly mentioned achievement of Byrne et al. research [7] was also accomplished by Versteijlen et al. with two conceptually different methods. Even though both were based on FEA results to calibrate an effective 1D model, one method engaged only lateral springs [27] , while the other employed both lateral and rotational types of springs [26], to represent soil reactions.

The latter research can be considered as the most rigorous because the 1D effective model is nonlocal. This means that the global nature of the soil response is not only incorporated, but also represented in the developed finite difference (FD) model. This, successively, means that the distributed lateral and rotational springs are fully coupled. Furthermore, the stiffness kernels of the method are obtained in a direct manner and afterwards can be used independently for design simulations. The drawback of this method is that it was developed for linear elastic soil properties. The last assumption of the method is considered correct for the very small strain regime[4], but it is known that the soil stress-strain relation is nonlinear[24].

1.3. Objective of the research

The previous paragraphs made clear that the *p-y* approach is not capable of capturing the SSI mechanisms developing when rigid behavior of monopile foundations is observed. However, the reduced computational time that a 1D model offers is highly desired. Even though, different approaches have been proposed in literature, only the nonlocal method of Versteijlen et al. [26] precisely represent the coupled soil response.

The method was developed assuming linear elastic soil properties. However, soil responds in a nonlinear manner. Furthermore, it is common to visualize the response of a laterally loaded MP by two curves, namely the horizontal force head[1] displacement and the overturning moment head rotation curves. These incorporate the nonlinear soil response and can be calculated with the assistance of 3D FEA. Hence, a question rises :

[1] The term head refers to the monopile at the mud-line level

"Is it feasible for a nonlocal 1D model to match the lateral force head displacement and overturning moment head rotation curves of a nonlinear 3D model?"

A positive answer to this question means that a faster and simpler 1D model can accurately predict the response, under quasi-static loading, of a MP foundation in nonlinear soil. The computational time reduction may not be extensive when the simulations are time independent. Nevertheless, it would prove that a nonlocal model can be expanded to nonlinear applications. This is a first step on the way of incorporating nonlinear SSI in the design of monopile foundations for offshore wind turbines.

1.4. Outline

This section describes the structure of this report. First of all, in Chapter 2 the nonlinear nonlocal 1D effective model is described. In this chapter firstly an introduction of the 1D model is presented, followed by the governing equations that represent it. Subsequently, the stiffness parameters are explained and the computational procedure is depicted in a generic manner. Next, the expansion of the stiffness matrices to a 3rd dimension (planes), with which the nonlinear soil response is captured, is analyzed. Finally, the misfit functions, which quantify the quality of the 1D effective model, are presented.

The nonlinear nonlocal 1D effective model is based on 3D FEA results. These simulations are necessary to incorporate the 3D soil effects in the model and are specified in Chapter 3. The beginning of the chapter is devoted to explanations regarding material properties, element types and meshing techniques, which concern the 3D FE model. Afterwards, a description of the simulations needed to compute the stiffness terms for the 1st plane of the matrices (representing the undisturbed soil resistance) of the nonlinear nonlocal 1D effective model is illustrated. After, three methods for 3D simulations that could produce the other planes are explained. The chapter is finalized with a discussion regarding two critical topics concerning nonlinear effects on the procedure.

The results of the study are shown in Chapter 4. Firstly, results regarding the 1st plane of the matrices are documented and examined in contrast with a literature example. The selection of the approach concerning the 3D simulations, yielding to the other planes of the matrices, is followed by findings referring to the nonlinear 3D stiffness matrices. After the interpolation techniques used in the nonlinear nonlocal 1D effective model are discussed, the chapter is summarized by final results in terms of lateral force head displacement and overturning moment head rotation curves.

Finally, the conclusions of the research and recommendations for improving the nonlinear nonlocal 1D effective model are offered in Chapter 5.

2

The Nonlinear Nonlocal 1D Effective Model

The nonlinear nonlocal 1D effective model is inspired and expands the extensive work of W.G. Versteijlen on the the subject [26]. This chapter focuses on describing the applied nonlinear nonlocal 1D effective model. The uniqueness of the model is that the global behavior of the continuum is precisely represented. This is achieved by employing nonlinear fully coupled lateral and rotational springs representing the SSI. Moreover, the stiffness kernels of these springs incorporate all the 3D effects, because they are extracted from 3D FEA. The chapter starts with the general concept of the model, followed by the mathematical representation. Before the 3rd dimension (planes) of the stiffness matrices, capturing the nonlinear behavior, is introduced, the nonlocality is described. The chapter is finalized by the means of quantification of the quality of the nonlinear nonlocal 1D effective model.

2.1. General concept

The large-diameter MP foundations behave rigidly to lateral loads. This behavior, successively, mobilizes a large volume of the continuum generating a global (nonlocal) response of the soil. Moreover, soil is known for the nonlinear relation between stress and strain [24]. Therefore, the fundamental principle of the nonlinear nonlocal 1D effective model is to precisely represent both the nonlocality and the nonlinearity of the SSI with MP foundations.

This 1D model is based on Timoshenko beam theory, assuming it is founded on a distributed, Winkler-type foundation, which consists of two fully coupled types of springs, lateral and rotational. More elaborate explanation of the stiffness kernels of these springs follows on the next sections (Sections 2.2, 2.3 and 2.4).

This model is developed for quasi-static combinations of horizontal force and overturning moment at the mud-line level. It can predict deflection, slope, rotation and curvature along the length of the pile. Its performance is quantified by misfit functions described in Section 2.6.

2.2. Governing equations of the 1D model

In the previous section it was mentioned that the nonlinear nonlocal 1D effective model is based on Timoshenko beam theory. The next equations describe the response of the system, the first illustrates force and the second moment equilibrium.

$$GA\kappa\left(\frac{d^2u(z)}{dz^2} - \frac{d\psi(z)}{dz}\right) - f(z,u,\psi) = 0 \tag{2.1}$$

$$GA\kappa\left(\frac{du(z)}{dz} - \psi(z)\right) + EI\frac{d^2\psi(z)}{dz^2} - m(z,u,\psi) = 0 \tag{2.2}$$

Regarding the equations, G is the shear modulus of steel, A is the cross sectional area, κ represents the Timoshenko shearing coefficient (which for the cylindrical shape of the monopile a value of 0.53 is presumed), while E is the Young's modulus and I the second moment of area on the x direction (Figure 2.1). The last term in both equations is the soil resistance, in terms of distributed lateral force and bending moment respectively. The sign convention of the 1D model is illustrated on Figure 2.1, which also shows the soil resistance in the form of springs.

To fully define the 1D model, boundary conditions are also necessary. The internal shear force is equal and opposite to the external force, both at the top and at the end of the beam. Moreover, the internal bending moment is equal to the external moment, both at the top and at the end of the beam . The shear force equilibrium is described by eqs. (2.3) and (2.5), while eqs. (2.4) and (2.6) refer to the moment equilibrium. Note that at the tip of the pile the external force and moment are assumed to be zero, which is opposite to the discrete shear and moment tip resistance concept introduced by Byrne et al [6].

$$GA\kappa\left(\frac{du(z)}{dz} - \psi(z)\right)\Big|_{z=0} = -F \tag{2.3}$$

$$EI\frac{d\psi(z)}{dz}\Big|_{z=0} = M \tag{2.4}$$

$$GA\kappa\left(\frac{du(z)}{dz} - \psi(z)\right)\Big|_{z=L} = 0 \tag{2.5}$$

$$EI\frac{d\psi(z)}{dz}\Big|_{z=L} = 0 \tag{2.6}$$

The introduction of the boundary conditions makes the model well defined, but the soil resistance is in very general terms. Firstly, the lateral resistance is discussed. The term global (nonlocal) soil reaction implies that every movement in the soil domain influences the SSI. Timoshenko beam equations describe the displacement of the MP using two variables. One is the lateral displacement on the *x* direction (u) and the other is the angle of rotation normal to the length of the pile (ψ), see Figure 2.1 for sign convention. The outcome of these two facts is the establishment of two types of stiffness representing the lateral SSI with the monopile, $K_{l,l}(z,\bar{z})$ and $K_{l,r}(z,\bar{z})$. The former stands for lateral stiffness because of deflection, while the latter for lateral stiffness due to rotation of the pile respectively. One of the independent variables (z) represents the dependence on the depth the stiffness is evaluated at. The other ($\bar{z}$) symbolizes the dependence of the stiffness on the deformed situation at other depths, signifying the (coupled) nonlocal soil response.

Similarly, the rotational resistance is also due to rotation and lateral deflection of the pile. Therefore, two more forms of stiffness are brought in, namely the rotational stiffness due to rotation of the pile ($K_{r,r}(z,\bar{z})$) and rotational stiffness on account of the deflection($K_{r,l}(z,\bar{z})$) of the pile. The use of z and $\bar{z}$ are identical with the lateral types of stiffness.

Finally, the aforementioned dependence on the disturbed situation along the depth ($\bar{z}$) implies an integration over the depth. The length of the pile is sufficient for this integration. The reason lays in the way the stiffness kernels are derived. They are based on reaction forces extracted from 3D FEA, which already incorporate the global (extended below the tip of the pile) soil response, refer to Section 2.3 for a more detailed explanation. Combining the above-mentioned with eqs. (2.1) and (2.2), eqs. (2.7) and (2.8) are derived.

$$GA\kappa\left(\frac{d^2u(z)}{dz^2}-\frac{d\psi(z)}{dz}\right)-\int_0^L K_{l,l}(z,\bar{z})u(\bar{z})d\bar{z}-\int_0^L K_{l,r}(z,\bar{z})\psi(\bar{z})d\bar{z}=0 \quad (2.7)$$

$$GA\kappa\left(\frac{du(z)}{dz}-\psi(z)\right)+EI\frac{d^2\psi(z)}{dz^2}-\int_0^L K_{r,r}(z,\bar{z})\psi(\bar{z})d\bar{z}-\int_0^L K_{r,l}(z,\bar{z})u(\bar{z})d\bar{z}=0 \quad (2.8)$$

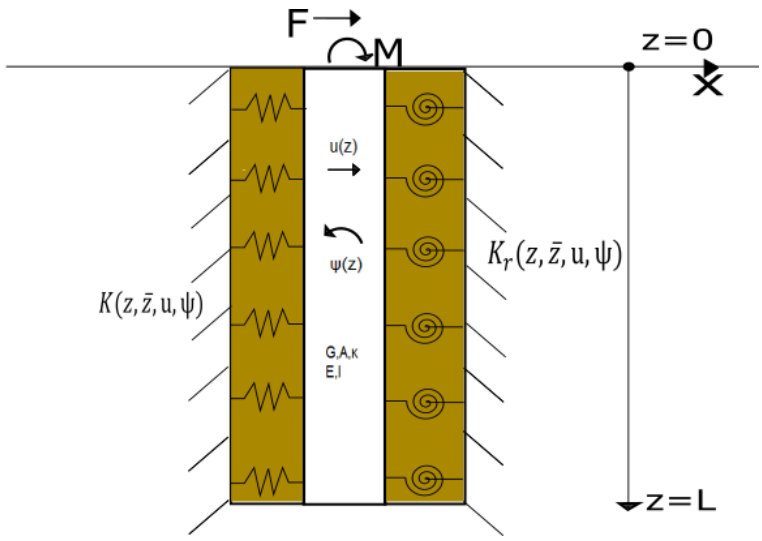

Figure 2.1: Schematic representation of the 1D beam model

2.3. Soil stiffness from 3D FEM

So far the introduced model is described by continuous equations. However, when implementing discrete results of FEA into another model, spacial discretization of the equilibrium equations is obligatory. The result is that the continuum variable z is transformed to a vector $\boldsymbol{z}$[1], which implies that all the terms of eqs. (2.7) and (2.8) are vectors or matrices. At this point, it is important to mention that the 1D effective model follows the vertical discretization of the 3D FE model (see Section 3.1.2 for 3D meshing information).

The stiffness matrices are now represented by [n+1,n+1] matrices (n being the ratio of pile length over discretization height), in order to incorporate the nonlocality of the soil response. How the nonlocality is introduced in the stiffness matrices is explained with the assistance of the lateral-lateral stiffness matrix, $\boldsymbol{K}_{l,l}$:

Later, Section 2.4, it will get explained that the stiffness matrices are expanded in a 3rd dimension. Therefore, they are described by rows, columns and planes. The following process is employed for determining all the planes. Extracting each plane of $\boldsymbol{K}_{l,l}$ is established on displacement-based simulations (see Figure 2.2). The number of the simulations needed for every plane is $(n+1)$. The circumference of

[1]Bold symbols represent vector or matrix

the pile geometry is composed by rings of nodes along the depth. The first simulation requires restraining all the degrees of freedom (DoFs) of all these nodes except for the nodes at the mud-line. These are horizontally displaced by a specific uniform amount. The second, demands all the nodes of the circumference to be restrained, apart from the ring at a depth equal to the vertical discretization. This ring is also subjected to the same disturbance. The same process is followed for all the rings. In all *(n+1)* simulations, the lateral reaction forces on all the nodes of the geometrical circumference of the pile are gathered (together with the vertical reaction forces and the displacement field of the pile). For every discrete depth, the horizontal forces of these nodes are summed and form a column of a force matrix ($\boldsymbol{F_x}$), also [n+1,n+1].

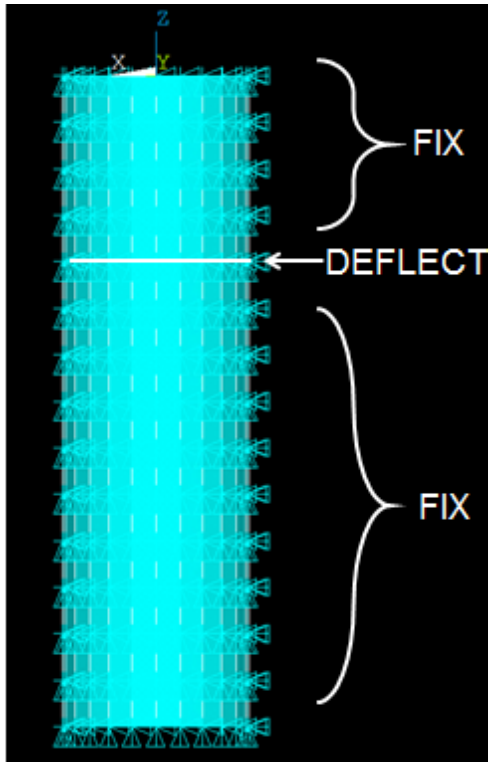

Figure 2.2: Illustration of the model for the perturbation phase

Except for forces, displacements are necessary when stiffness is to be computed.

For all the $(n+1)$ simulations, the lateral displacement of the pile is different, because the perturbation is imposed at another depth. Each deformed shape is collected to a column of the displacement matrix ($\boldsymbol{U}$ [n+1,n+1]). Moreover, the displacement matrix has to incorporate the calculation of the integral of equation 2.7. Therefore, a matrix ($\bar{\boldsymbol{U}}$) which includes the Trapezium rule for integration, i.e. every cell is multiplied by the discretization length and the first and last row of the matrix is halved, is employed.

Translating the aforementioned into matrix notation, assuming we refer to the j^{th} simulation we get the following :

$$f_{x,i}^{j^{th}} = \sum_{l=1}^{m} f_{x,i,l}^{j^{th}} \qquad \begin{aligned} \bar{U}_{z=0}^{j^{th}} &= \frac{1}{2} h U_{z=0}^{j^{th}} \\ \bar{U}_{z=i}^{j^{th}} &= h U_{z=i}^{j^{th}} \\ \bar{U}_{z=L}^{j^{th}} &= \frac{1}{2} h U_{z=L}^{j^{th}} \end{aligned}$$

$$\boldsymbol{f_x^{j^{th}}} = \left.\begin{matrix} f_{x,1}^{j^{th}} \\ \cdot \\ f_{x,i}^{j^{th}} \\ \cdot \\ f_{x,n+1}^{j^{th}} \end{matrix}\right\} n+1 \; rows \qquad \bar{\boldsymbol{U}}^{\boldsymbol{j^{th}}} = \left.\begin{matrix} \bar{U}_{z=0}^{j^{th}} \\ \cdot \\ \bar{U}_{z=i}^{j^{th}} \\ \cdot \\ \bar{U}_{z=L}^{j^{th}} \end{matrix}\right\} n+1 \; rows$$

$$\boldsymbol{F_x} = \overbrace{\begin{bmatrix} \boldsymbol{f_x^{1^{st}}} & . & . & . & \boldsymbol{f_x^{(n+1)^{th}}} \end{bmatrix}}^{n+1 \; columns} \qquad \bar{\boldsymbol{U}} = \overbrace{\begin{bmatrix} \bar{\boldsymbol{U}}^{\boldsymbol{1^{st}}} & . & . & . & \bar{\boldsymbol{U}}^{\boldsymbol{(n+1)^{th}}} \end{bmatrix}}^{n+1 \; columns}$$

$$\boldsymbol{F_x} = \left.\overbrace{\begin{bmatrix} \cdot & \sum_{l=1}^{m} f_{x,1,l}^{j^{th}} & \cdot \\ \cdot & \cdot & \cdot \\ \cdot & \sum_{l=1}^{m} f_{x,n+1,l}^{j^{th}} & \cdot \end{bmatrix}}^{n+1 \; columns}\right\} n+1 rows \; \bar{\boldsymbol{U}} = \left.\overbrace{\begin{bmatrix} \cdot & \frac{1}{2} h U_{z=0}^{j^{th}} & \cdot \\ \cdot & \cdot & \cdot \\ \cdot & h U_{z=i}^{j^{th}} & \cdot \\ \cdot & \cdot & \cdot \\ \cdot & \frac{1}{2} h U_{z=L}^{j^{th}} & \cdot \end{bmatrix}}^{n+1 \; columns}\right\} n+1 rows$$

where i refer to a random depth along the vertical discretization of the pile, m represents the number of nodes per ring and n the ratio of pile length over discretization height.

Note that at eqs. (2.1) and (2.2) the response of the model is described per unit length. Hence, the extracted forces should all get divided by the discretization length. Thus, the equation to get solved for deriving $\boldsymbol{K_{l,l}}$ (lateral-lateral stiffness matrix) is :

$$\frac{1}{h}\boldsymbol{F_x} = \boldsymbol{K_{l,l}}\bar{\boldsymbol{U}} \Leftrightarrow \boldsymbol{K_{l,l}} = \frac{\boldsymbol{F_x}\bar{\boldsymbol{U}}^{-1}}{h} \tag{2.9}$$

The collected vertical forces find application in computing the rotational-lateral stiffness matrix, $\boldsymbol{K_{r,l}}$. These vertical forces multiplied by the distance of every node from the centerline of the pile equal the rotational resistance (moment). Following similar steps for the moment matrix, the equation for determining $\boldsymbol{K_{r,l}}$ is :

$$\boldsymbol{K_{r,l}} = \frac{\boldsymbol{M_y}\bar{\boldsymbol{U}}^{-1}}{h} \tag{2.10}$$

In addition, following an analogous procedure, imposing rotation instead of horizontal displacement, the remaining stiffness matrices (rotational-rotational and lateral-rotational stiffness matrices) can be calculated.

$$\boldsymbol{K_{r,r}} = \frac{\boldsymbol{M_y}\bar{\boldsymbol{\Psi}}^{-1}}{h} \tag{2.11}$$

$$\boldsymbol{K_{l,r}} = \frac{\boldsymbol{F_x}\bar{\boldsymbol{\Psi}}^{-1}}{h} \tag{2.12}$$

Concluding, the direct benefit of the process is the introduction of the nonlocality. This is achieved by collecting reaction forces along the length of the pile, even though the perturbation is at a discrete specific depth. The reaction forces on the restrained rings illustrate the continuity of the soil domain (nonlocality). The upcoming section introduces the nonlinearity of the 1D effective model, while the next chapter elucidates the process.

2.4. Introduction of the nonlinearity

In this research, the 3D FEA include soil modeled with a nonlinear constitutive model (see Section 3.1.1). This means that a nonlinear relation exists between the loading on the monopile and the respective displacement. The same nonlinear relation should also be captured in the 1D effective model. Therefore, the stiffness matrices are extended to a third dimension, which describes this dependence of the response on the loading magnitude.

This third dimension consists of planes that are calculated exactly as described before, but in different equilibrium positions of the monopile. The term equilibrium position refers to a state of displacement field. This is a deformed shape introduced by loading the monopile at the mud-line level with a combination of a lateral force and an overturning moment. Therefore, the lateral and rotational perturbations are imposed not only on the undeformed shape of the pile, giving the first plane of the 3D matrices (0^{th} equilibrium position), but also on deformed shapes offering extra planes of these matrices (see Figure 2.3). To make things clearer, the meaning of a

random cell on the lateral-lateral stiffness matrix ($K_{l,l}(i,j,k)$,$1 \leq i,j \leq L/h+1$) is described. This cell represents the part of lateral stiffness at depth of $(i-1)\cdot h$ (h the vertical discretization), which is coupled with the displacement at a depth $(j-1)\cdot h$ for the $(k-1)^{th}$ equilibrium position. The exact loading combination responsible for this position depends on the case under examination, but the process to select them is explained in the next section.

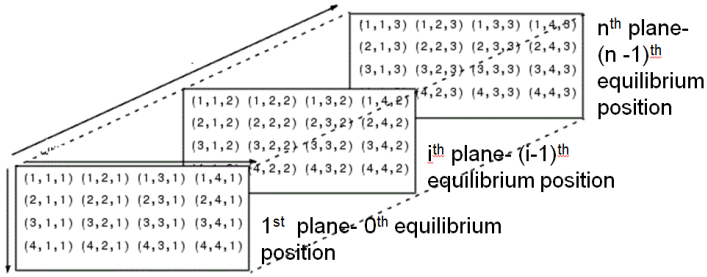

Figure 2.3: Schematic illustration of the stiffness matrices

2.5. Selection of the equilibrium positions

The equilibrium positions at which the planes of the stiffness matrices are computed are case sensitive. The selection is based on results of incrementally increasing lateral load of a 3D SSI simulation.

First of all, the fundamental objective of the nonlinear nonlocal 1D effective model is to predict the response on high loads. Thus, it was decided to keep the ratio of applied overturning moment over lateral force at the mud- line level constant, at a potential ULS level. More specifically, this ratio (the lever arm) is taken as 40 for the reference case.

The magnitude of the lateral force must also be determined. For this purpose two representative stiffnesses are derived: the generalized pile head lateral and rotational stiffness. The first is computed as the ratio of lateral load over displacement of the monopile at the seabed. The second is calculated as overturning moment over rotation again at the same elevation. After deriving these quantities for a range of lateral loading, there is an indication of the model's (lateral and rotational) stiffness evolution with respect to the applied lateral load.

It was considered that the important load magnitudes, at which the planes of the stiffness matrices are computed, are those which are necessary to approximate

(using the wavelet compression [15]) both of the aforementioned evolutions, see Figures 2.4 and 2.5, with a tolerance of 1%. To clarify, the relative difference between the computed generalized stiffness values and the respective derived from the approximation is at maximum 1%. The points needed to accomplish such an approximation correspond to magnitudes of force, for which the stiffness matrices will be determined. Lower values of tolerance would lead to a higher amount of equilibrium positions, increasing the computational time significantly. However, as it would be discussed later on, Section 4.4.2 ,more equilibrium positions may be required for improving the accuracy of the process, indicating that either a smaller tolerance or a different selection process is required.

2.6. Misfit functions

Tis section describes the functions that quantify the quality of the nonlinear nonlocal 1D effective model. The target of the 1D effective model is the 3D response along the length of the pile, despite the fact that the guidelines focus on limits for the pile head displacement[10]. Its performance is evaluated by four misfit functions. One assesses the quality of the fit based on the deflections, one on the slope, one on the rotation and one on the curvature (u, u', ψ, ψ' respectively). These misfit functions are defined by the eqs. (2.13) to (2.16), but can be summarized by the summed value (Eq. 2.17). The one fourth on the definition of every misfit function is an assumption of equal weight factor [26].

$$C_u = \frac{1}{4}\frac{\sum_{i=1}^{n+1}|u_{i,1d}-u_{i,3d}|}{\sum_{i=1}^{n+1}|u_{i,3d}|} \quad (2.13) \qquad C_{u'} = \frac{1}{4}\frac{\sum_{i=1}^{n+1}\left|u'_{i,1d}-u'_{i,3d}\right|}{\sum_{i=1}^{n+1}\left|u'_{i,3d}\right|} \quad (2.14)$$

$$C_\psi = \frac{1}{4}\frac{\sum_{i=1}^{n+1}|\psi_{i,1d}-\psi_{i,3d}|}{\sum_{i=1}^{n+1}|\psi_{i,3d}|} \quad (2.15) \qquad C_{\psi'} = \frac{1}{4}\frac{\sum_{i=1}^{n+1}\left|\psi'_{i,1d}-\psi'_{i,3d}\right|}{\sum_{i=1}^{n+1}\left|\psi'_{i,3d}\right|} \quad (2.16)$$

$$C_{tot} = C_u + C_{u'} + C_\psi + C_{\psi'} \quad (2.17)$$

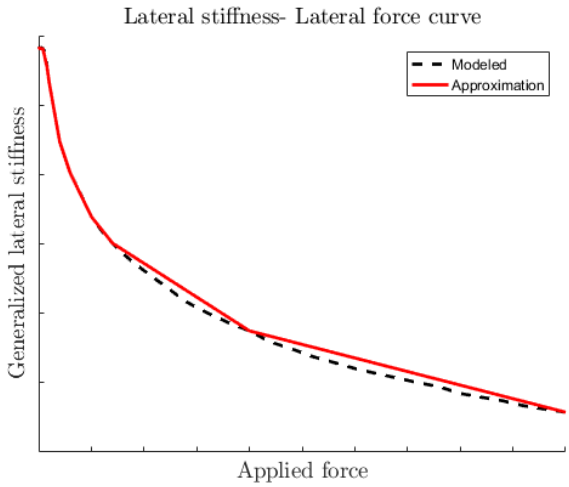

Figure 2.4: Lateral load selection based on generalized lateral stiffness

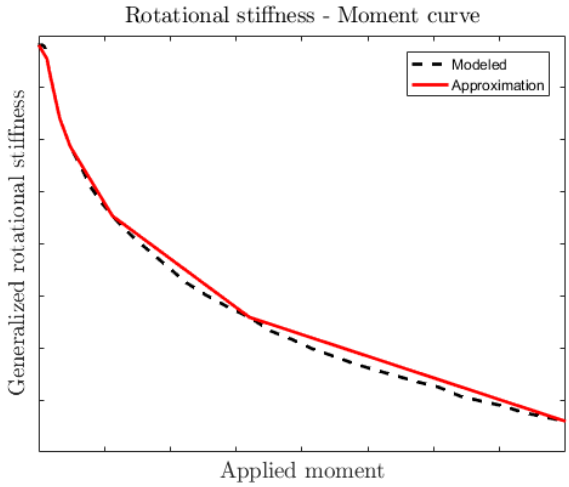

Figure 2.5: Lateral load selection based on generalized rotational stiffness

3

3D Simulations

This chapter presents the process followed in the 3D simulations. At the beginning, information regarding the 3D modeling technique adopted in this project is offered. Afterwards, the approach for the 0^{th} equilibrium position is depicted. Next, three different approaches for the other equilibrium positions are described. Finally, two critical topics related to nonlinear effects on the procedure are discussed. With the end of the chapter, the exact steps of the 3D modeling will be clear. Moreover, the reader will gain insight on the procedure followed when calculating the stiffness matrices of the nonlinear nonlocal 1D effective model.

3.1. General information

First of all, the commercial software Ansys Structural v18.2 was used for the 3D simulations. The constitutive material models for soil are to some extent limited in Ansys. However, the last few years more alternatives are available and version 18.2 includes the Mohr-Coulomb (MC) option.

3.1.1. Soil constitutive model and element types

Even though MC is a relatively simple model when describing soil response, it contains the basic soil failure criterion (Figure 3.1) and is commonly used. Moreover, it is the first attempt to produce a nonlinear nonlocal 1D effective model and it is presumed that if it can be established on a simple nonlinear constitutive model, it could later be upgraded with more advanced and sophisticated constitutive soil models. Hence, MC was employed for modeling the nonlinear soil behavior in Ansys.

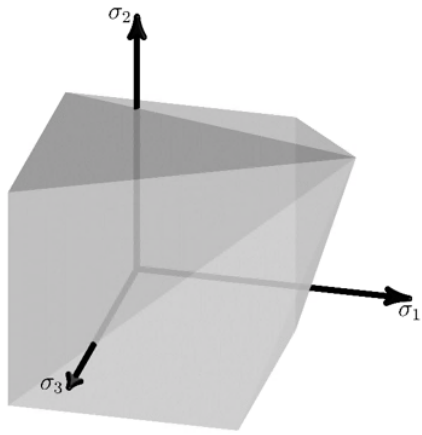

Figure 3.1: MC yield surface in principal stresses space (positive sign implies tension)[3]

Both examined soils in this research are homogeneous sands. Thus, tension cut-off was applied, since the sandy soils are known for not having tensile strength. Furthermore, effective density of the soil was considered. The reason behind this is firstly the fact that any alteration of stress is due to change of effective stress [25] and secondly the nature of sandy soils. The latter implies the assumption of instantaneous dissipation of the pore pressure, meaning that the external load is directly transfered to the soil skeleton. Thus, only the effective part of the geostatic stresses was considered.

As stated before, the considered soils are homogeneous sands, with properties summarized in Table 3.1 (Case 1 is considered to be the reference case of this study). According to Poulos [20] if the pile flexibility factor is smaller than 0.0025 the response of the monopile can be called flexible, while if it is larger than 0.208 the response can be considered rigid. As it can be seen on the the aforementioned table, the first combination is categorized as intermediate pile behavior, neither rigid nor flexible, while the second as rigid pile. Ansys provides the option of reducing the soil strength after yielding, but it was decided to keep the strength parameters (c, ϕ) constant. The dilatancy angle mentioned on the table is used for the calculation of the plastic flow, which is non associated [3]. On the other hand, the monopile was modeled with linear elastic material, the properties of which are specified on Table 3.2.

Parameter	Units	Case 1	Case 2
Effective density (ρ')	kg/m^3	1000	1000
Effective Young's Modulus (E')	MPa	79.7	20
Friction angle (ϕ)	°	38	30
Dilatancy angle (ψ)	°	8	0
Cohesion (c)	kPa	0.1	0.1
Pile flexibility factor[1] (K_r)	-	0.0625	0.25

Table 3.1: Soil properties

Parameter	Units	
Diameter (D)	m	8
Length (L)	m	28
Thickness (t)	mm	75
Young's Modulus (E)	GPa	210

Table 3.2: Monopile properties

Finally, the types of element used in the simulations are mentioned. The soil domain was modeled with SOLID185, while the pile with SHELL181. The former type is a brick element defined by 8 nodes with three translational degrees of freedom (DoFs) at each node. The latter is a shell element with 4 nodes, having three translation and three rotational degrees of freedom per node.

3.1.2. Meshing and calculations

In order to reduce computational time, taking advantage of the plane symmetry, only half of the space was modeled. Regarding meshing, close to the monopile it is structured and relatively fine, while further away in the domain mesh can be free and coarser. Moreover, since the procedure is for the first time established in nonlinear soil properties and the time required for the simulations increases significantly with finer meshing, the vertical discretization close to the pile was chosen to be 2 meters. The reason for this increase is firstly the additional nodes. The second and more important reason is that every ring of nodes describing the circumference of the monopile will get displaced both laterally and rotationally for every equilibrium position and the finer the discretization the more rings are to be displaced. It should

[1] $K_r = \frac{EI_p}{E_s L^4}$, EI_p being the bending stiffness of the pile, E_s the Young's modulus of soil and L the length of the pile

be reminded here that the vertical discretization of the pile at the 3D model coincides with the vertical discretization of the 1D model. A typical example of a meshed model is available on Figure 3.2. Lastly, the applied boundary conditions are noted. At the bottom of the domain, all the DoFs are fixed, at the circumference the DoFs related to the horizontal plane are constrained, while for the plane of symmetry the perpendicular to this plane displacement is restrained.

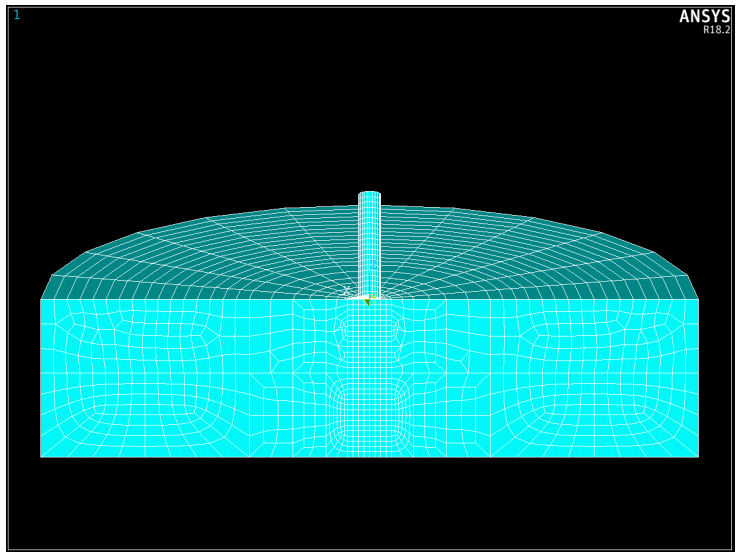

Figure 3.2: Typical meshed model

In addition, the connection between monopile and soil elements is described. Even though there is the option of introducing contact elements in-between the two kind of element, which would allow "sliding" or "gapping", it was decided to make this connection rigid, so as the model is relatively simple. Moreover, it is known that the interaction between soil and pile elements is less strong than between soil elements and it had been stated that the skin friction angle (δ) could be considered equal to 2/3 of the internal friction angle (ϕ) [25]. This means that close to the pile a material with less strength should be incorporated. However, in this study homogeneous soil material properties were used even close to the pile, in order the 3D model to remain simple.

Furthermore, regarding the loading combination on the monopile, the moment at mud-line is imposed by applying a lateral load at a height of 40 m above this level

at the centerline of the monopile. In order to achieve a smooth transition of the point load to the monopile elements, the nodes at the top of the monopile and the node at which the load is applied are rigidly connected.

Two more subjects are to be discussed. The first refers to the geostatic stress calculations. The general nature of Ansys comes with a consequence on this gravitational loading, the produced displacements. This displacement field is coupled with the stress field, but it occurred many years ago and it would be unnatural to include it on the analysis. Thus, a maneuver to eliminate the displacement but keep the stress field was applied. However, small residual displacements remain in the soil domain.

Finally, the second subject concerns the size of the soil domain. It is known that the boundaries of the domain should not influence the results of the analysis. However, larger model requires more computational time. Therefore, a balance between these two must be achieved. For this scope, a mesh convergence analysis was conducted and it was decided that there is no need for a domain larger than 30 times the monopile radius, as it can be seen at Figure 3.3. Lastly, the depth of the domain was chosen to be slightly larger than double the length of the pile.

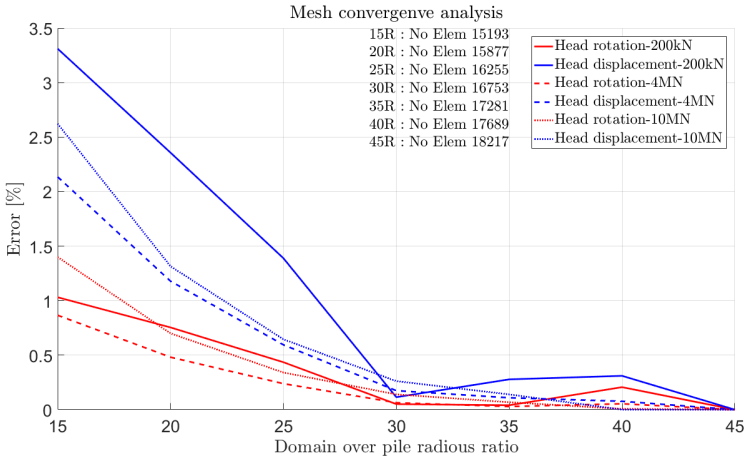

Figure 3.3: Mesh convergence analysis results

3.2. 0^{th} Equilibrium position

This equilibrium position produces the first plane of the stiffness matrices and refers to the undeformed shape of the pile. As it was shown by eqs. (2.7) and (2.8),

the stiffness matrices represent pure soil stiffness, because the stiffness of the steel monopile is incorporated in the other terms of these equations. In general, this requirement created some challenges on the 3D modeling, but not for this equilibrium position simply because there is no need the monopile to be modeled, as no pre-stress due to the pile displacement needs to be taken into account.

In the previous work of W.G. Versteijlen [26] it is clearly mentioned that the volume of the steel should be replaced by "cavity". However, this gap would cause misalignment with the next equilibrium positions, because the monopile is modeled with shell elements associated with "virtual" thickness. Therefore, it was decided to keep this volume filled with soil.

To summarize, the 3D model for the 0^{th} equilibrium position is a pure soil model, at which first the geostatic stress field is imposed. Afterwards, lateral and rotational perturbation is independently enforced to all the ring of nodes, as described at Section 2.3.

3.3. Next equilibrium positions

The stiffness matrices in the nonlinear nonlocal 1D effective model represent pure soil stiffness. Therefore, lateral and rotational disturbances are to be imposed in a 3D model which excludes the pile stiffness. Moreover, these perturbations are enforced on a deformed shape, introduced by a load combination on the monopile at the mud-line level. This means that in the 3D simulations there should be phases of loading that include the stiffness of the pile and others where it should be excluded. Changing the stiffness of a FE model influences either the force or the displacement field, because of the generic relation $F = K \cdot u$. Due to the complexity of this situation, several approaches were developed and tested. The upcoming subsections are discussing this effort. They are presented in the order they got developed. The main reason for the development of every next method was to increase the accuracy of the nonlinear nonlocal 1D effective model. More elaborate reasoning on the approach selection follows in Section 4.2.

Table 3.3 summarizes the level of loading for every equilibrium position, for both the examined cases. The nonlinear behavior of soil starts from very small loading. Therefore, as it was expected, the selection of equilibrium positions is denser on the region of "small" loading rather than in the region of "large" loads.

Table 3.3: Equilibrium positions for the two cases

Case1	**F [kN]**	60	140	200	600	800	1.2e3	2e3	3.6e3	6e3	10e3
	M [MNm]	0.24	5.6	8	24	32	48	80	144	240	400
Case 2	**F [kN]**	160	200	400	600	1e3	1.4e3	2e3	4e3	10e3	-
	M [MNm]	0.64	8	16	24	40	56	90	160	400	-

Although the approaches differ, they all start from the same point. First of all, there is a model with the geostatic stress and the pile wished in place, because no installation effects are taken into consideration in this study. To make the upcoming sections more comprehensible every model is associated with a name. This normal SSI 3D model will be called the "starting-point" model. Afterwards, a lateral load is applied at the top of the monopile, which would give a deformed shape, see Figure 3.4, at which the perturbations will later be imposed. At this point, the stiffness of the monopile should be removed from the model, and that is where the distinction of the approaches is introduced. The last loading phase of the "starting-point" model is schematically illustrated on Figure 3.12 and is the starting point of all the upcoming approaches.

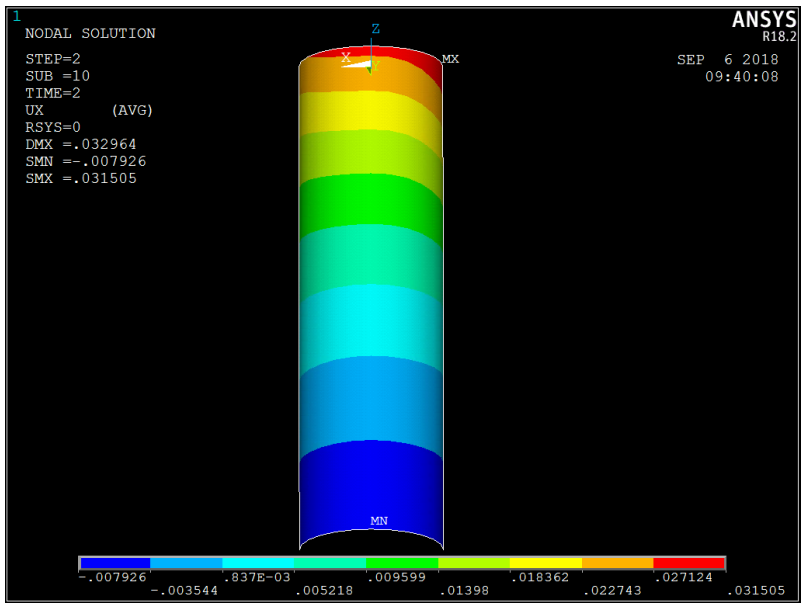

Figure 3.4: Indicative pile displacement in the loading direction- F = 6MN- Case 1

3.3.1. The "subtraction" approach

As mentioned before, all these approaches have been developed so as at the end the pure soil resistance can be computed. The characteristic of the "subtraction" approach is that the resistance of the linear elastic steel material can be calculated separately and subtracted later on from the combined resistance. Therefore, the perturbations are imposed to the "starting-point" model and the reaction forces (on the x and z direction according to Figure 3.2) on the nodes of the pile are gathered, illustration in Figure 3.5. Furthermore, the same magnitude of perturbation is enforced to an extra model, which includes the same monopile but founded on a linear elastic soil with Young's modulus of 1 Pa, so that its stiffness can be neglected: a "pile on air" model, Figure 3.6. The former model is considered to compute the combined resistance while the latter the monopile's resistance. Hence, the difference of the forces of the two models would represent the pure soil resistance.

Lastly, a final comment on this approach should be made. This method requires the perturbation simulations to be applied at two models for every equilibrium position. However, due to the well-known superposition principle of linear systems[29], it is considered that the analyses of "pile on air" is adequate to be performed at the undeformed shape of the monopile only. These results (forces) can afterwards get subtracted from the final results of the "starting-point" model for every equilibrium position.

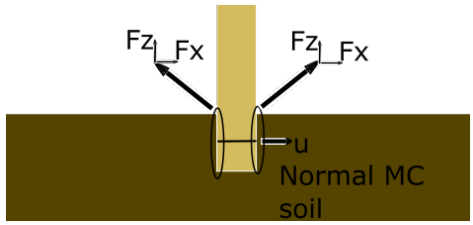

Figure 3.5: Schematic representation of the perturbation phase for the "starting-point" model

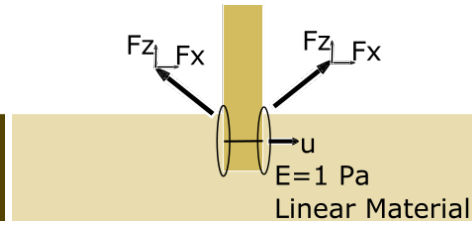

Figure 3.6: Schematic representation of the perturbation phase for the "pile on air" model

3.3.2. The "rational" approach

This method is also developed with two models. To be more precise, the first is the "starting-point" model and there is no extra loading phases on it. The second is the "pure soil" model, a model with only soil elements. The special features of this approach are the way the "pure soil" model was created and the loading phases imposed to it.

First of all, the pure soil model was created so as there is perfect correspondence of nodes, elements, materials etc. with the "starting-point" model, excluding the elements of the monopile. This exact agreement is necessary because results of the one model are transfered to the other. Possible results that could be imposed to the "pure soil" model are displacements or forces on the nodes. The overall stiffness of the model is much smaller (due to the absence of the pile), thus enforcing forces on the nodes would create erroneous displacement field and consequently inaccurate stress field. Therefore, it was decided that the displacement field of the whole domain of the "starting-point" model would be gathered (Figure 3.7).

These results (displacement field) are imposed to the "pure soil" model as constrains and the nodal reactions forces are collected (Figure 3.8). This transfer of the displacement field from one model to another already introduces small discrepancy in the stress field. Moreover, by constraining the nodes of the model an obvious problem rises. If all the nodes are fixed how will the upcoming load phases be introduced?

The solution to this problem has already been indicated. All the nodes of the model are released (except for the boundaries support), but the just computed nodal reaction forces are enforced (Figure 3.9). This step is a source of a small distortion of the deformed shape of the pile. In order the significance of the exact shape of the MP to be examined, an alternative third step of this method was developed. This is to keep the shape of the monopile fixed and simultaneously impose the reaction nodal forces on the remaining domain (Figure 3.11). Finally, as always the last step is applying the perturbations, Figure 3.10.

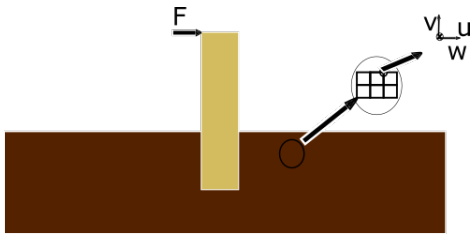

Figure 3.7: Schematic representation of the 1st step of the "rational" approach - Gather displacement field from "starting-point" model

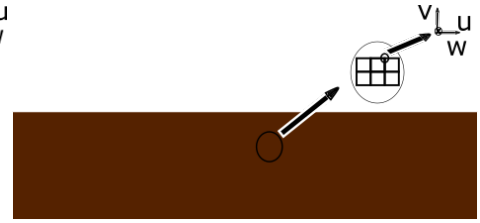

Figure 3.8: Schematic representation of the 2nd step of the "rational" approach - Impose displacement filed on the "pure soil" model

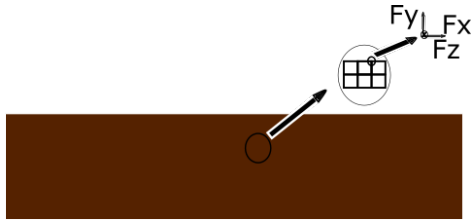

Figure 3.9: Schematic representation of the 3rd step of the "rational" approach- Impose force field on the "pure soil" model

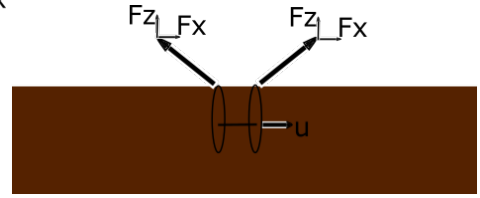

Figure 3.10: Schematic representation of the 4th step of the "rational" approach - Impose perturbations on the "pure soil" model

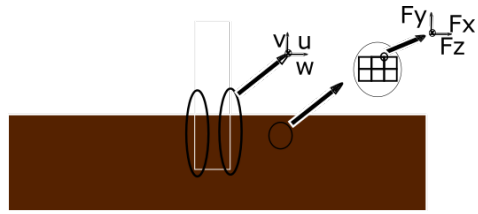

Figure 3.11: Schematic representation of the alternative 3rd step of the "rational" approach - Impose force field & keep the shape of the monopile nodes fixed with respect to each other on the "pure soil" model

3.3.3. The "effective" approach

The uniqueness of this process is the utilization of only one model, the "starting-point". Ansys gives an option for deactivating elements of the model in the different calculation phases. Therefore, after applying the lateral load at the monopile, Figure 3.12, the steel elements are deactivated while the remaining domain is fixed, Figure 3.13. The reason for these constrains is to keep the displacement field unchanged, even though the stiffness of the domain had been altered. Afterwards, the nodes are released, with the exception of the circumference of the pile and the boundaries of the domain, while the nodal reaction forces are enforced, Figure 3.14. Finally, the perturbations are imposed, Figure 3.15.

The benefit of using only one model, no need to transfer data between models,

comes with a consequence. All the loading phases must be subsequent (otherwise data needs to be transfered), even though the horizontal perturbations are independent from the rotational. On the other hand, this independence can reduce the computational time when employing the "rational" approach because the simulations for the two kinds of disturbance can be simultaneous.

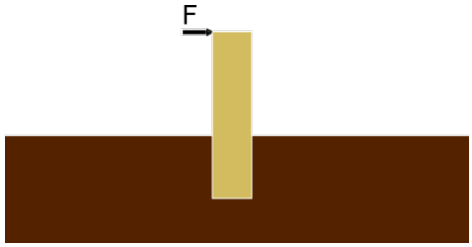

Figure 3.12: Schematic representation of the last loading phase of the "starting-point" model- Lateral loading- 1st step of the "effective" approach

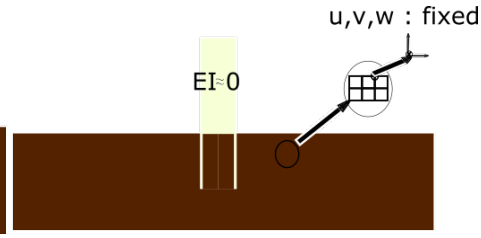

Figure 3.13: Schematic representation of the 2nd step of the "effective" approach - Deactivate the pile

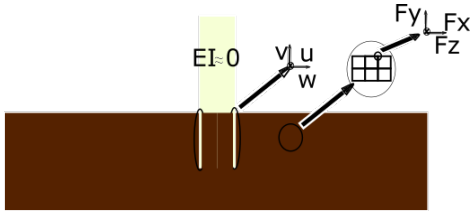

Figure 3.14: Schematic representation of the 3rd step of the "effective" approach - Impose force field & keep the shape of the monopile nodes fixed with respect to each other

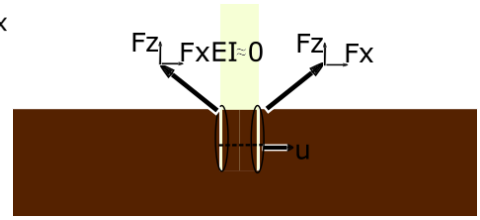

Figure 3.15: Schematic representation of the 3rd step of the "effective" approach - Impose perturbations

Concluding the section, a clarification regarding the calculation of the stiffness matrices is offered. Independently of the followed approach, they are produced by using total final forces (incorporating all the load phases) acting on the nodes, combined with the total final displacement. This decision was driven by the idea of

employing stiffness matrices that would resemble secant terms. If an analogy is made with a simple single degree of freedom mass founded on a nonlinear spring, the reason is more comprehensible. The response to a quasi-static incremental loading of the 1 DoF system would look like Figure 3.16. It can be seen that in order to linearize and predict a random displacement, a secant stiffness connected to the final force is used. Extrapolating and adjusting this fact to the examined case, total forces and displacements were considered the correct values.

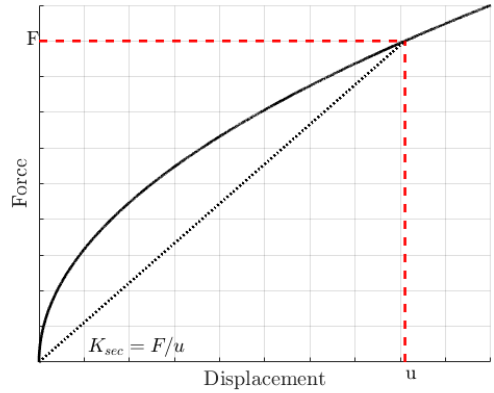

Figure 3.16: A quasi-static force displacement curve of a 1 DoF system founded on a nonlinear spring for quasi-static incremental loading

3.4. Effects of nonlinear behavior in the procedure

Although the process of the ring perturbation has been described in perfect correspondence with the description of W. G. Versteijlen [26], there are two small but crucial differences that have not been discussed until now. The first is regarding the direction of the perturbation and the second concerns the magnitude of it. Both of the topics became significant because of the nonlinear soil properties.

Firstly, the influence of the directionality of the perturbation is examined. Figure 3.17 illustrates a typical deflection and rotation distribution over depth of a laterally loaded monopile. It can be seen that regarding rotations the sign is constant over the depth while as far as the deflections are concerned there is a change of sign.

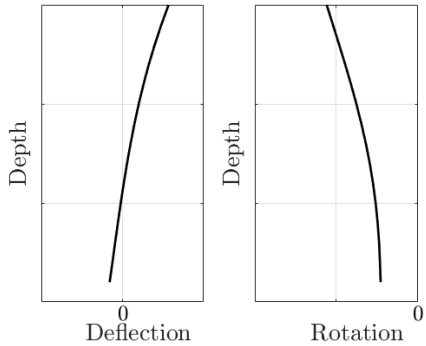

Figure 3.17: Typical deflection and rotation distribution of a laterally loaded pile

The perturbation should not be an unloading phase for soil domain. Thus, the imposed disturbances should have the direction of the deflected shape. To clarify, for the rotary perturbation on the rings, a rotation in the same direction along the length of the pile is imposed, because the soil behavior (together with the sign of rotation on the MP) is consistent along the depth. On the other hand, as far as the horizontal displacements are concerned they are enforced towards the positive direction above the rotation point of the monopile, while below the center of rotation towards the negative direction, following the deflected shape.

Secondly, the magnitude of the perturbation is discussed. The fundamental idea at the beginning of the study was to apply a small in magnitude perturbation so as the soil domain is as lightly as possible distorted and the stiffness matrices are representative for the load combination of each equilibrium position. Therefore, it was selected the lateral displacement to be $0.01mm$, while the rotary motion equal to $10^{-5}rad$. In order to check if the perturbations are small enough, it was decided to compare the results of these analyses with results of simulations with double these magnitudes.

Figures 3.18 and 3.19 illustrate this comparison for the 0^{th} equilibrium position. First of all, the former graph is discussed. At the 0^{th} equilibrium position each ring is independently horizontally displaced by $0.01mm$ and the local lateral forces on the every time deflected ring are collected and added. The procedure is exactly the same to what it was described in Section 2.3, but the forces only at the displaced rings are of interest. Hence, every depth is represented by a value of perturbation (always $0.01mm$) and a value of force. Moreover, the same process is followed at an independent set of simulations, but with a horizontal disturbance of $0.02mm$. The

perturbation ratio, between the two sets of simulations, is displayed on the left subplot of Figure 3.18 and of course is constantly 2 along the length of the pile since these displacements have been imposed. On the right subplot of the same figure the ratio of the "local" reaction forces on every ring is illustrated, which, with the exception of the first meters close to the boundaries of the domain, are also perpetually 2. Consequently, the imposed lateral displacement is small enough, because double magnitude of action creates double magnitude of reaction meaning that the response is linear and no nonlinearities were introduced due to the perturbation. Analogously, by applying rotations of $10^{-5}rad$ and $2 \cdot 10^{-5}rad$ and gathering instead of lateral, vertical forces (which multiplied by their distance from the centerline of the monopile give restoring moments) Figure 3.19 is produced. It can be seen again that the reaction is proportional to the action thus the imposed rotation is adequately small.

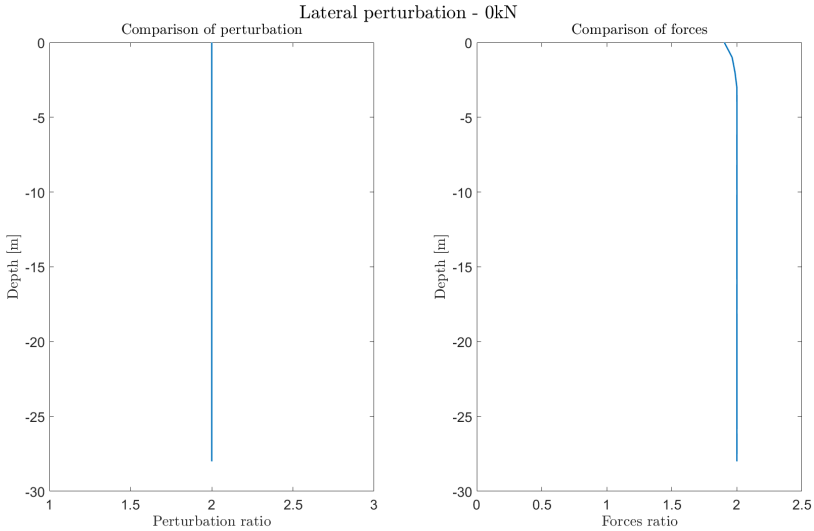

Figure 3.18: Lateral perturbation and lateral local force ratio along the length of the pile at the undeformed shape

Unfortunately, the previously mentioned comparison is not enough to prove that the magnitude of perturbation is appropriate for all the equilibrium positions. Hence, the same process has been followed for other equilibrium positions as well. Figures 3.20 and 3.21 illustrate the comparison for horizontal perturbations around equilib-

rium positions of a relatively low and a relatively high lateral load. In the former situation it can be observed that for perturbations at relatively large depth (where the deflections are small and the strength high) the response is still linear, however closer to the top where the deflections are high and the strength small the response is not linear any more. Regarding, the latter load it is obvious that the response is far from being linear. The reason for the nonlinear response, even on equilibrium positions of small loading, is that the soil elements in touch with the displaced nodes are subjected to intense shear. Furthermore, shearing is a type of loading that can cause failure to soil elements, thus nonlinear response. Nonetheless, it must be said that the applying small magnitude of perturbations has not been proven erroneous either.

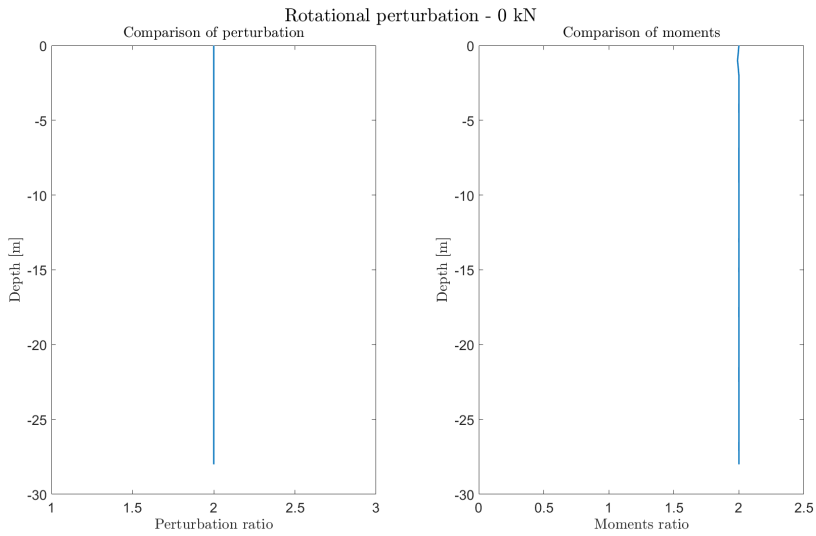

Figure 3.19: Rotational perturbation and local moment ratio along the length of the pile at the undeformed shape

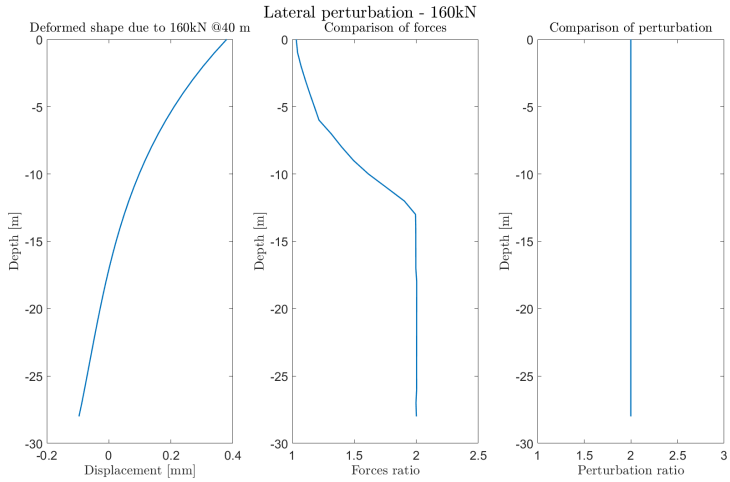

Figure 3.20: Lateral perturbation and lateral local force ratio along the length of the pile at the equilibrium position of 160kN

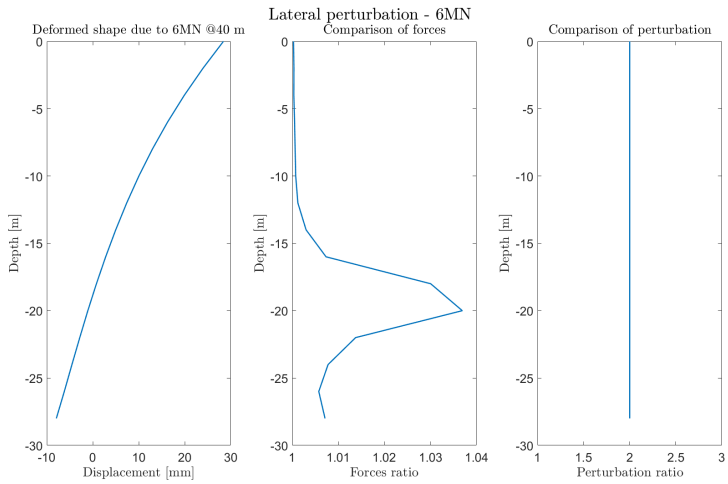

Figure 3.21: Lateral perturbation and lateral local force ratio along the length of the pile at the equilibrium position of 6 MN

Trying to decide what the appropriate magnitude of perturbation is, another comparison was also examined. It was decided to compute the stiffness matrices, at one equilibrium position, for different magnitudes of perturbation and compare the solutions of the nonlinear nonlocal 1D effective model. The different magnitudes are shown on Table 3.4 and the results are illustrated on Figure 3.22. It can be seen that the smaller the perturbation the better the results of the 1D effective model. The negligible difference between the $1 \cdot 10^{-5}$and $2 \cdot 10^{-5}$ indicates that a smaller magnitude is not necessary. Concluding, it was selected to continue the process with perturbations of $1 \cdot 10^{-5} m$ and $1 \cdot 10^{-5} rad$.

Type of perturbation	**Units**				
Lateral	m	$1 \cdot 10^{-5}$	$2 \cdot 10^{-5}$	$1 \cdot 10^{-4}$	$1 \cdot 10^{-3}$
Rotational	rad	$1 \cdot 10^{-5}$	$2 \cdot 10^{-5}$	$1 \cdot 10^{-4}$	$1 \cdot 10^{-3}$

Table 3.4: Magnitudes of perturbation that were tested

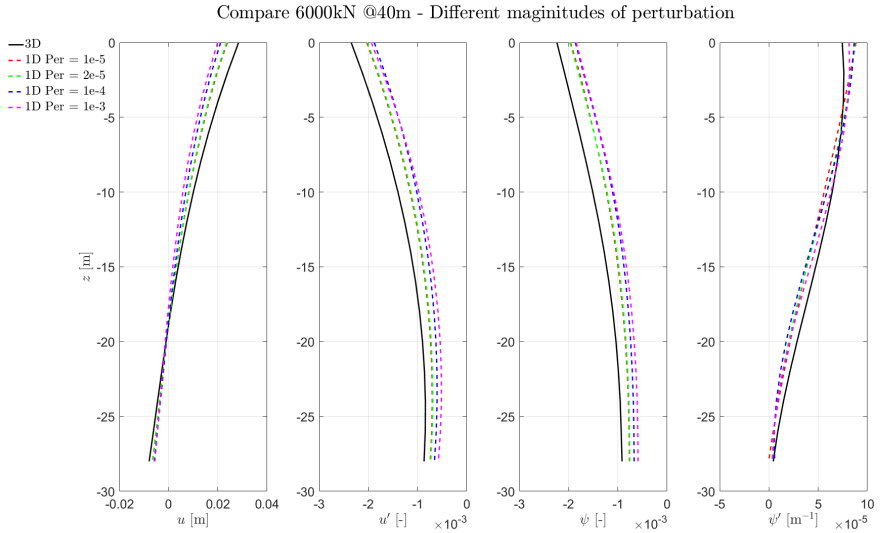

Figure 3.22: Performance comparison for different magnitudes of perturbation - 6 MN

4

Results

The chapter presents the outcomes of the study. Firstly the focus is on the 0^{th} equilibrium position topic. Next, results of the different approaches are shown, compared and the best approach is selected. Afterwards, intermediate findings are explained and a discussion on whether the results can be interpolated to intermediate load cases follows. Finally, the total and combined results are depicted.

4.1. "Linear Regime"

This section presents findings regarding the stiffness matrices of the 0^{th} equilibrium position. All the following figures refer to Case 1 since it is considered to be the reference case of this study. First of all, the same configuration holds for all the figures. To clarify, the columns of all the matrices run on the i direction while the rows on the j. Moreover, the cells of the first row refer to the mud-line level, whereas the cells of the last row indicate the tip of the monopile.

The focus now shifts to Figures 4.1 and 4.2. These illustrate the lateral-lateral stiffness matrix and the rotational-rotational stiffness matrix respectively. It can be seen that the shape resembles the results of W.G. Versteijlen [26]. The values of the main diagonal, representing the "local" stiffness, are high. The term "local" stiffness refer to stiffness at a specific depth connected to the deflection at the same depth. Moreover, the remaining non-diagonal values, representing the coupling of the continuum (nonlocality) are significantly lower. The magnitude of these cells may confusingly seem to be zero, but it is not.

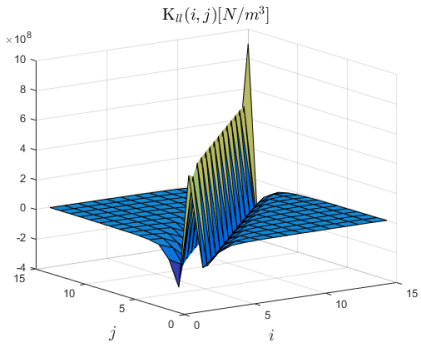

Figure 4.1: Lateral-lateral stiffness matrix- Case1 - 0 kN

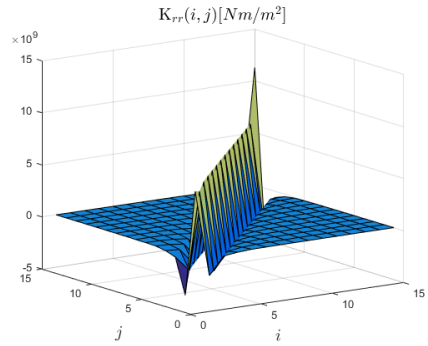

Figure 4.2: Rotational-rotational stiffness matrix- Case1 - 0 kN

Figure 4.3 provides assistance so as insight regarding the diagonal values of the under discussion matrices is gained. In the top left subplot the evolution of the "local" lateral resistance over the length of the pile is illustrated. To make things clearer an example is given. The value of the *x* axis at -10 m is the summation of the lateral forces acting on the ring at this depth, when this specific ring is displaced. The same explanation holds for every value on this line.

It can be observed that the magnitude is more or less constant with the exception of areas close to the boundaries of the monopile. This is rational because the stiffness of the soil, introduced to the 3D simulations by the Young's modulus, is constant over depth. As far as the top layers are concerned, it can be noticed that for the mud-line level the restoring force is slightly less than half of the constant value. This can be explained by the absence of soil elements above this level which would create more resistance in combination with the small strength of the top layers (correlation with Figure 3.18 at which the ratio of forces on these layers is not exactly 2). Moreover, this smaller strength at the top layers is to be blamed for the slightly smaller value at -2 m. Furthermore, the part close to the tip of the pile is to be discussed. At the tip level it can be noted that the resistance is smaller. A justification for this phenomenon is that the ring below is not constrained, when the ring of nodes at the tip is displaced. The auxiliary displacement matrix, which is not shown, is diagonal having the same value (the imposed perturbation), and incorporating the trapezium rule of integration. Therefore, the evolution of the "local" lateral stiffness evolves as depicted on the top right subplot. Following an analogous reasoning the bottom part of the figure, referring to the "local" rotational stiffness, can be explained.

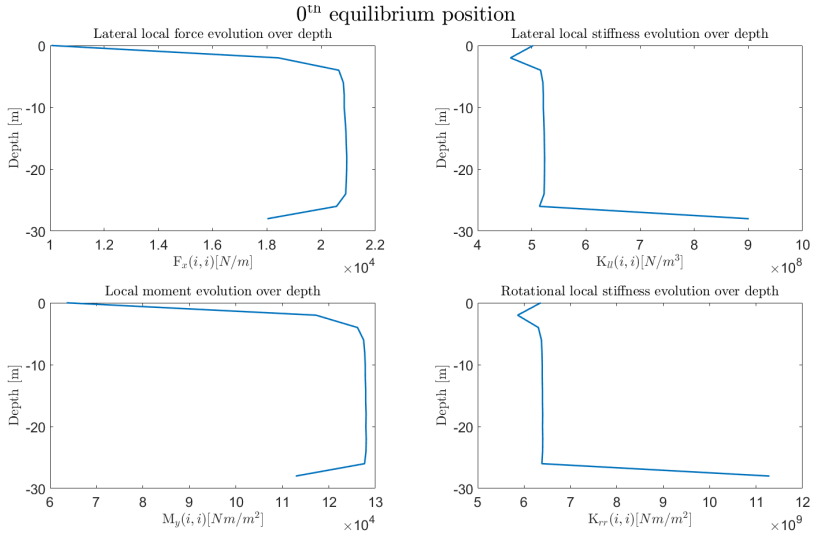

Figure 4.3: Evolution of the main diagonal for the lateral-lateral and rotational-rotational stiffness matrices

The coupling stiffness matrices, illustrated on Figures 4.4 and 4.5, are yet to be examined. The former figure refer to lateral resistance because of rotation, while the latter to rotational resistance due to deflection.

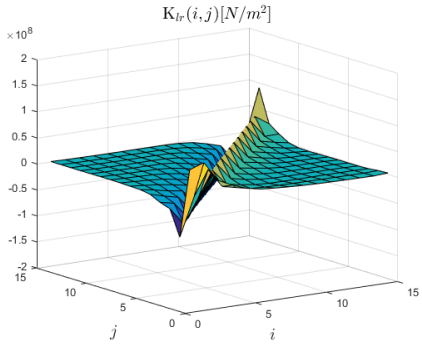

Figure 4.4: Lateral-rotational stiffness matrix- Case1 - 0 kN

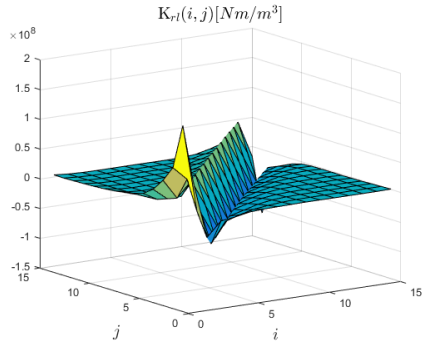

Figure 4.5: Rotational-lateral stiffness matrix- Case1 - 0 kN

The shape for both relates to the results of the study by W.G. Versteijlen [26]. However, especially at the layers close to the boundaries of the pile, discrepancies can be noticed. The exact relation $K_{l,r}(i,j) = K_{r,l}(j,i)$ reported in [26] is not found, but nonetheless the general behavior is similar.

Concluding, the results of the 0^{th} equilibrium position are described here so as an insight is offered and confidence on the process is gained by the comparison with the work of W.G. Versteijlen [26]. However, due to the effects of nonlinear soil behavior little will these stiffness matrices be used on later calculations.

4.2. Approach selection

All the different approaches examined in Section 3.3 were considered to be a solution on the problem of removing the stiffness of the monopile from the 3D model. However, the most appropriate way is yet to be decided. Since all seemed to be correct, the most preferred will be chosen by comparing the performance of the nonlinear nonlocal 1D effective model when employing every methodology.

Before the final selection is made, it is fruitful to visually compare the lateral-lateral stiffness matrices of an equilibrium position. For instance, Figure 4.6 illustrates these matrices calculated at the equilibrium position of 2 MN. All the approaches end up to similar shapes for the examined stiffness matrix. This enhances the belief that all the proposed methodologies are conceptually correct.

Examining the matrices of Figure 4.6 in more detail, there are two main differences between the “subtraction” approach and the others. Firstly, the diagonal value at the mud-line level for the “subtraction” approach is significantly smaller than what is derived with the other methods. Secondly, it seems like the negative stiffness on the first column representing the coupling of the continuum is smaller in absolute value compared with the respective of the other approaches.

The complexity of simulations do not allow intuitive reasoning. However, a difference between this method and the others, which could introduce these dissimilarities, is that this method includes 3D models that continue above the seabed, while for the alternative methodologies there is no stiffness at elevation higher than the mud-line. Indicatively, Figure 4.7 shows a comparison of 3D and 1D results based on the “subtraction” approach. It can be seen that the 1D model gives a much stiffer response, therefore this approach is considered inappropriate.

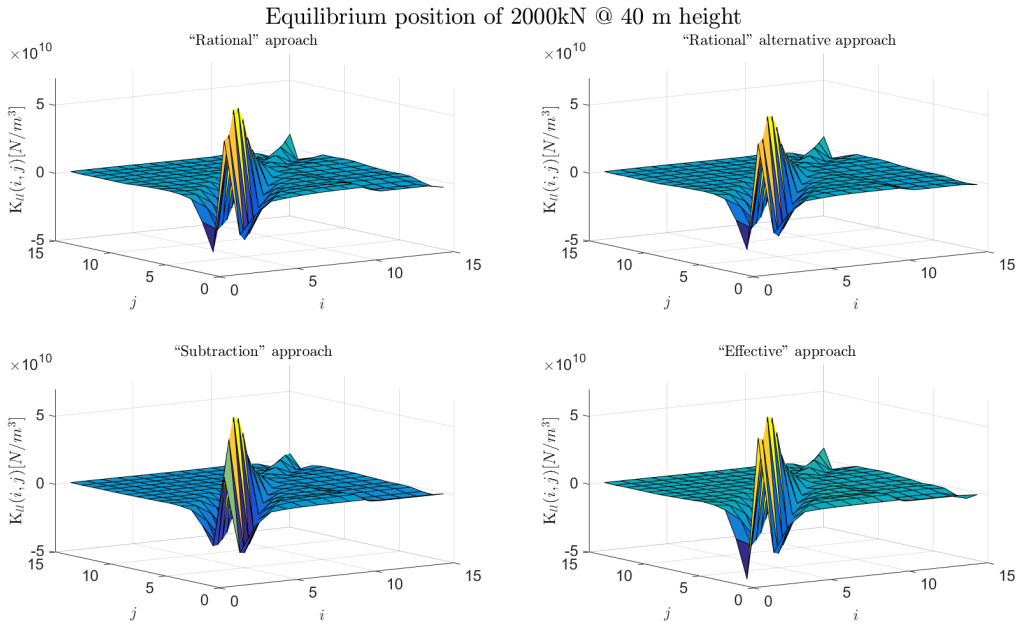

Figure 4.6: Lateral-lateral stiffness matrices for the different approaches - Case1 - Equilibrium position of 2 MN

The results of the other methods are satisfying, but it would be too extensive to document the results for every equilibrium position for all the methods. Therefore the 1D solutions are summarized in a lateral force - head displacement and an overturning moment - head rotation curve, available on Figures 4.8 and 4.9.

In the aforementioned figures, it can be noticed that in the majority of points, the alternative "rational" approach gives a better approximation. Thus, it was concluded that the retainment of the exact shape of the monopile is important. This was the reason that the "effective" approach was developed integrating this finding. Moreover, it can be observed that the 3D solution is approximated more accurately when employing the "effective" approach, especially in high loads.

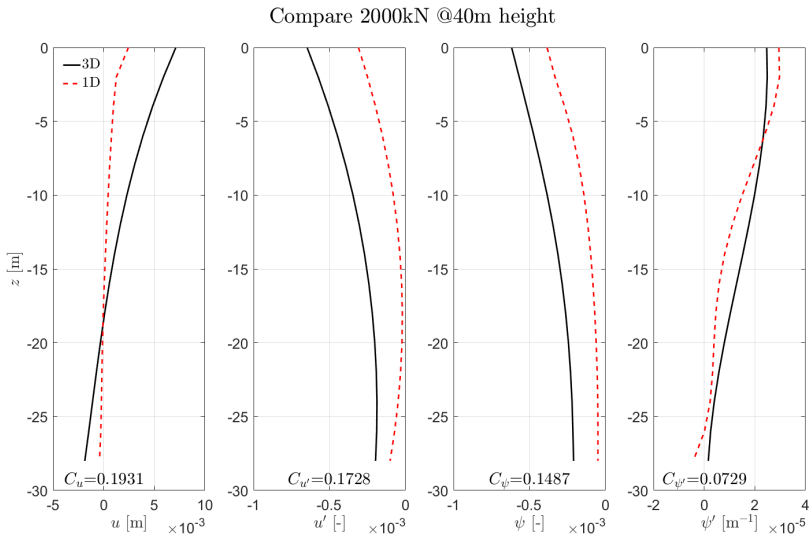

Figure 4.7: Comparison of 3D and 1D results using the "subtraction" approach - Case 1

The main reason for the dominance of this approach is the benefit of working with one FE model. To elucidate, when transferring the displacement field from one model to another discrepancies are introduced and the higher the magnitude of the displacements the larger the error. However, it can be expected that with finer discretization these dissimilarities are to be mitigated.

To summarize this section, it can be confirmed that the "subtraction" approach did not produce the expected results. On the other hand, the other methodologies approximate adequately the 3D solution. However, the best approximation occurs when employing the "effective" method. Thus, the study, from now on, focuses on results of this methodology exclusively.

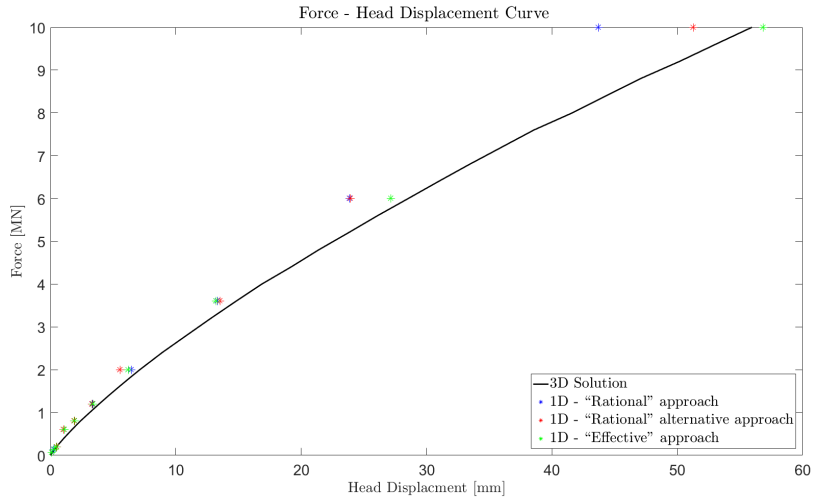

Figure 4.8: Comparison of the methods based on force displacement curve

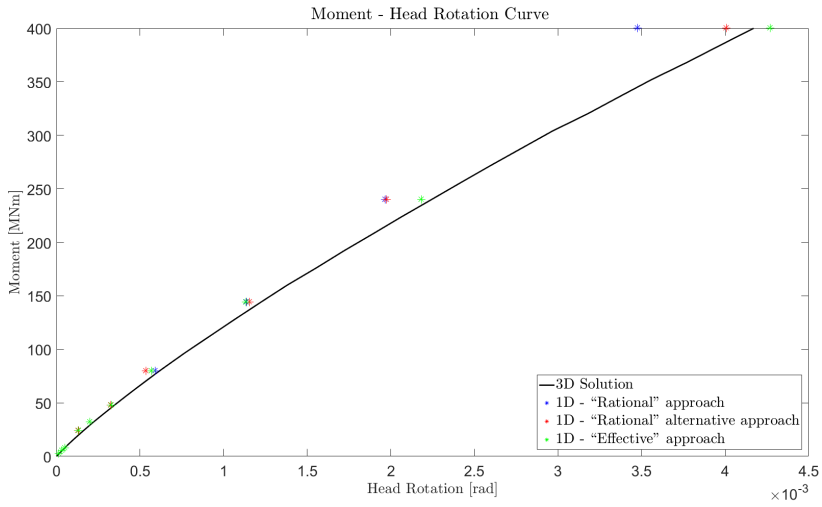

Figure 4.9: Comparison of the methods based on moment rotation curve

4.3. Equilibrium positions

This section focuses on results and findings regarding the other equilibrium positions. First of all, the performance of the nonlinear nonlocal 1D effective model on a high load is depicted. Indicatively the equilibrium position of 10MN, Figure 4.10, is presented here (all the comparisons are available on Appendix A). It can be seen that the 1D effective model is performing very well, with a total misfit of $C_{tot} = 2.7\%$. In comparison, W.G. Versteijlen had documented total misfits of $C_{tot} = 1.8\%$, $C_{tot} = 3.6\%$, $C_{tot} = 13.4\%$ and $C_{tot} = 7.3\%$ for the examined cases of his research [26]. Achieving similar total misfit value, when including nonlinear effects in the SSI, is considered an accomplishment of this study. However, the section is devoted at two findings regarding the behavior and the shape of the stiffness matrices. On the upcoming explanations the example of lateral-lateral stiffness matrix is used.

First of all, a detailed explanation of a lateral-lateral stiffness matrix is given. Comprehending the shape of such a matrix, as shown on the bottom right of Figure 4.6, is a complex task. Therefore, Figure 4.11 was produced to give an insight. This figure consists of three graphs. It should get reminded that each row of the force matrix refer to forces acting on the same ring, because of perturbations at different depths. On the other hand, each column represent forces over depth because of a disturbance at a specific depth. Once this is clear, it should be intuitive that when a row of the force matrix is plotted against depth, the coupling of soil reaction between the depth that this row represent and the other levels is illustrated. This is shown on the left graph of the aforementioned figure.

At first, the almost constant part of each line is discussed. This part clearly shows that the influence of perturbation is low at depths away from the level of disturbance. It can also be noticed that the magnitude of this part firstly increases until the second row and then decreases and becomes even negative. If this evolution is plotted against depth, it would create the distribution of lateral reaction force illustrated on the middle figure (blue line). The shape of distribution of the lateral force over depth is typical for a laterally loaded monopile and is in correspondence with the deformed shape shown in the same figure (black line). However, the summation of this distribution is not exactly equal to the external horizontal load creating this equilibrium position (6 MN). The reason is that the distribution also includes the (small) influence of the perturbation as well.

Moreover, the behavior of the peaks is explained. These represent extra force introduced by the perturbation. It can be seen that the relative increase of force is getting less as we approach the rotation point of the monopile, with the exception of the first two rows. This irregularity can be due to boundary effects and the small

strength of the top layers. However, the general trend can be explained by pre-stress effects. To clarify, the more the soil is pushed to one direction the more reaction is available on this direction until the limit of passive reaction is reached [24].

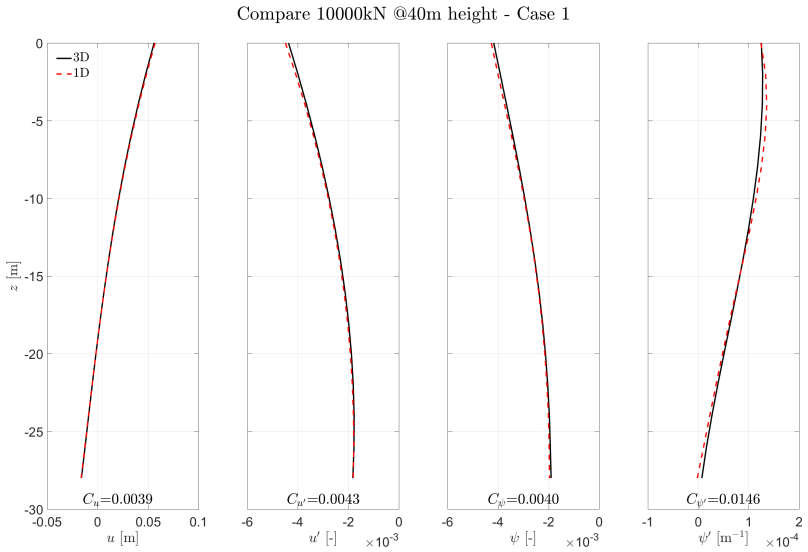

Figure 4.10: Comparison of the 1D effective model performance

Once the left figure is clear, the transition to the shape of the stiffness matrix, represented by the diagonal, the 4th row and the 4th column on the right graph, is possible. Each point of the diagonal is computed as the scalar product of every line of the left graph by the respective column of the inverse displacement matrix (including the trapezium rule of integration). These columns have negative values except for the row at which the perturbation is imposed until the rotation point, while the vise versa happens below it. An example of a column of this matrix for different equilibrium positions is available on Figure 4.14. The change of sign according to the position with respect to the rotation point is a consequence of disturbing the soil in the direction of the deformed shape. Therefore, the diagonal of the lateral-lateral stiffness matrix is as illustrated on the right graph of Figure 4.11 (magenda line)

As far as the line representing the 4th row of the matrix is concerned, each point is derived by the scalar product of the green line of the left graph with each of the columns of the inverse displacement matrix. Combining this with the information in

the last paragraph regarding the inverse displacement matrix, explains not only the peak but also the change of sign at the rotation point of the green line on the right graph. The explanation of the red line in the right graph is analogous.

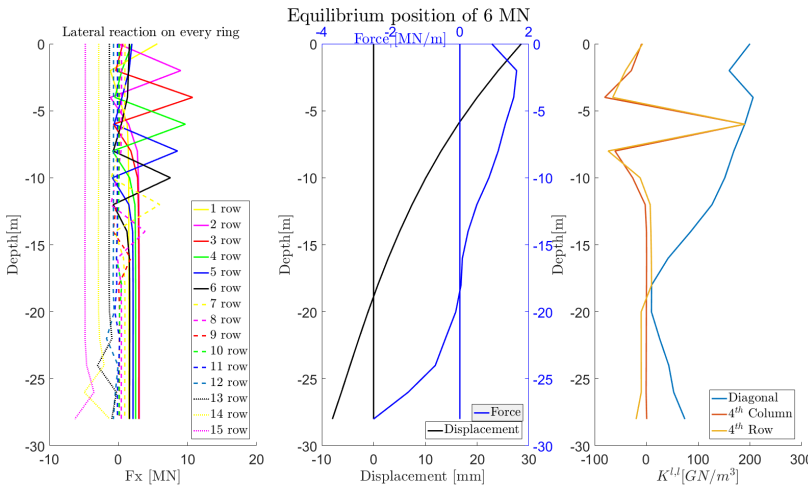

Figure 4.11: Explanatory graph for the shape of a lateral-lateral stiffness matrix

Another interesting observation is an increase of magnitude on the diagonal of the lateral-lateral and rotational-rotational stiffness matrices with increasing external loading at the equilibrium positions. Once more, the former matrix is used as explanatory example but the reasoning is similar for the latter as well.

The left graph of Figure 4.12 shows a similar to the left graph of Figure 4.11 plot. Here, however, only one row of the force matrix is plotted but for all the equilibrium positions. It can be seen that the constant part is increasing with higher external lateral load at the top of the pile. The external loading is rising, therefore soil reactions are also intensifying and this is illustrated by this increase. Furthermore, the magnitude of the peak climbs because of the same pre-stress effect that it was mentioned before. The scalar product of these rows with the 3rd column of the inverse displacement matrices (Figure 4.14) computes the stiffness for the cell $K_{l,l}(3,3)$. Hence, the magnitude of the lateral-lateral stiffness for the specific cell is increasing, as it can be seen on the middle graph. Generalizing, this behavior is occurring for all the cells of the diagonal, as is depicted on the right part of the below figure.

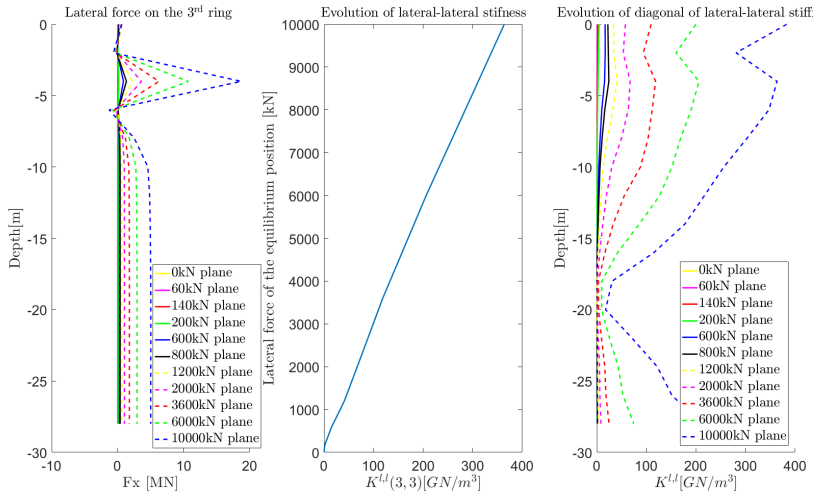

Figure 4.12: Explanatory graph for the behavior of the lateral-lateral stiffness matrices with increasing equilibrium position

4.4. Interpolation in between the planes

On the previous section, Figure 4.10 clearly shows that the developed nonlinear nonlocal 1D effective model can perform very well on high loads. However, this performance summarized on Figures 4.8 and 4.9 is only discrete points. The actual challenge for this model is to approximate the two curves entirely. Of course, the same procedure for calculating the stiffness matrices of the nonlinear nonlocal 1D effective model can be applied for every loading. However, such a process is not efficient because of the extensive computational time required. The solution to this is an effective interpolation.

It should get clear that the aforementioned interpolation is to be employed in-between the planes of all the stiffness matrices. Surface interpolation require a clear trend of evolution for the planes of the matrices. Such a trend can not be spotted, therefore it was decided to perform single entity interpolation. To clarify, the estimation of any stiffness value used on the nonlinear nonlocal 1D effective model is based on the evolution of a specific cell. For example, deriving values of the lateral-lateral stiffness matrix that refer to depth of -4 m connected to the displacement at -4 m for case 1, only the values $K_{l,l}(3,3,x), x = \mathbf{Z} \bigcap [1,11]$ are used. Remember that the vertical discretization of both examined cases is 2 m and 11

equilibrium positions are selected for case 1.

4.4.1. Single entity evolution

Efficient interpolation requires a good estimation of the evolution (in the 3rd dimension) of each cell. As it was shown and explained on the previous section a cell on the diagonal of $K_{l,l}$ or $K_{r,r}$ has an increasing in magnitude behavior when propagating from the 0th to the last equilibrium position. The behavior of other cells is still to be discussed.

Firstly, a cell just below the main diagonal of $K_{l,l}$ is examined. Figure 4.13 is similar with the left and central part of Figure 4.12. To clarify, on the left subplot the lateral forces acting at a depth of -6 m because of the perturbations over the length of the pile, for all the equilibrium positions, are illustrated. An example is given for clarification purposes. The point of the blue dashed line at the seabed level describes the force acting on the ring at -6 m because of displacing the ring at the seabed at the equilibrium position of 10 MN. The scalar product of every line on the left graph with the 3rd column of the inverse displacement matrix (including the trapezium rule of integration) calculates every point of the right graph, which is the evolution of $K_{l,l}(4,3)$ with increasing loading. As it can be seen in Figure 4.14 the difference of the aforementioned column with rising loading is negligible. Therefore, it can be claimed that the decrease of the examined cell is mainly due to the increase of the peak of the force on the ring at -6 m. This can be attributed to the already mentioned pre-stress effect.

Unfortunately, the monotonic behavior of the already examined cells is not always observed. As it can be seen on Figure 4.15 non-monotonic evolution may occur. This can be explained only if it is separated into smaller areas, where the mechanisms responsible for a change are detectable. Therefore, Figures 4.16, 4.17 and 4.18 are produced to assist on the explanation of this behavior.

First of all, the first of the three figures is discussed. On the left part of the graph, the deflection shape for the first five equilibrium positions of case 1 is shown. Moreover, rectangles representing the depths at which at least one soil element next to the pile has entered the perfectly plastic region (before imposing the perturbation) are illustrated.

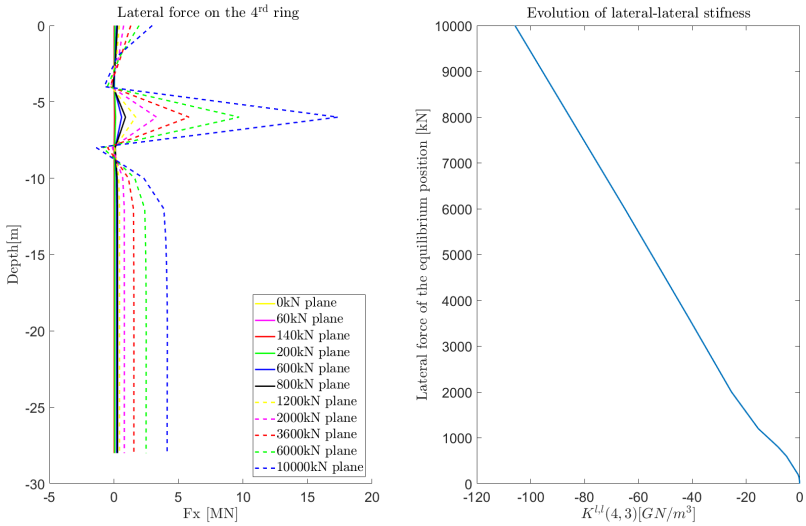

Figure 4.13: Behavior of $K_{l,l}(4,3)$ with increasing loading

To derive these areas the principal stresses of the soil elements attached to the monopile were extracted from the 3D FEA. Based on these principle stresses and the Mohr- Coulomb failure criterion generalized to any state of stress (Equation 4.1[3]) the yielding deviatoric stress of every element was calculated and compared with the acting stress. If the acting deviatoric stress was equal to the yield deviatoric stress the element was considered to have entered the plastic region. Mind that in Equation 4.1 compression is considered positive. Furthermore, p is the mean pressure, q_y the yielding deviatoric stress and θ the Lode's angle.

$$\frac{q_y}{\sqrt{3}}\left(cos\theta - \frac{sin\theta sin\phi}{\sqrt{3}}\right) = p \cdot sin\phi + c \cdot cos\phi \tag{4.1}$$

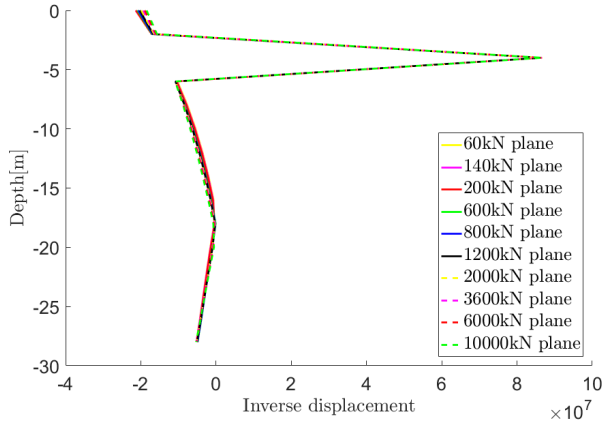

Figure 4.14: 3rd column of inverse displacement matrix with increasing loading

In the central part of Figure 4.16 the forces acting at a depth of -12 m because of disturbances over the length of the pile are plotted against the depth for respective equilibrium positions (similarly to the left graph on Figure 4.12). On the other hand, the right subplot illustrates the evolution of $K_{l,l}(7,3)$ with increasing loading.

A change on this evolution can be spotted in between 200 kN and 600 kN , where the stiffness changes sign. This can be explained by the central and left part of the figure. Remember that the relative difference of the column of the inverse displacement matrix is negligible especially for small loading (Figure 4.14). In the middle graph, it can be seen that the force distribution on the examined ring is similar up to the 200 kN equilibrium position, while it changes for the 600 kN case. This is the reason of the change in sign, but why is this alteration observed?

Answer can be given by the plastic regions illustrated on the left subplot. It can be noticed that the depth at which soil elements have been plastified is only until -4 m for loading of 200 kN. These elements are relatively far away from the examined depth, thus the influence on the force acting on the ring of nodes is small. In contrast, regarding the equilibrium position of 600 kN the plastification depth have reached much closer to the under discussion depth and the influence is more severe. Concluding, the behavior of $K_{l,l}(7,3)$ for relatively small loading is mostly influenced by the depth the plastification area has reached.

Figure 4.17 depicts the same kind of plots as Figure 4.16, but for higher loading. The configuration and the illustration are identical for the two graphs. In addition, on the left graph of the former figure the percentages illustrate the amount of plas-

tified elements attached to the pile. On the right part of the under discussion figure, it can be observed that the behavior changes twice in this range of loading. Remember that up to 600 kN the stiffness was increasing. This alteration is attributed to redistribution of forces.

Firstly, the decrease of stiffness up to the equilibrium position of 1.2 MN is examined. As it can be seen on the left part of the figure, for the equilibrium position of 600 kN the plastification area has not reached the under discussion depth (-12 m), while for external loading of 800 kN and 1.2 MN elements at this depth have entered the plastic region. Therefore, redistribution of forces occur, resulting in the reduction of stiffness.

On the other hand, from the equilibrium position of 1.2 MN to 2 MN an increase on the stiffness is observed. This can be justified by the increase of force at -4 m due to pre-stress effects. Moreover, the increase of plastified elements to almost 70% makes the redistribution of forces extensive. This complex phenomenon makes further explanations on this increase difficult to be given.

Finally, the depth at which elements have entered the plastic region for the 2 MN equilibrium position should be discussed. It is counter-intuitive the fact that plastification has occurred to elements at the rotation point, where the displacement is very small, while the elements in between -16 m and -18 m are still in the elastic region. This can be explained by the change of depth of the rotation point with increasing loading. As it can be seen on Figure 4.16 the rotation point is in between -16 m and -18 m , while only for loading greater than 600 kN the rotation point drops below - 18 m. Therefore, the accumulated shearing induced to the elements below -18 m is higher than the respective shearing in between -16 m and -18 m, which explains the plastification region.

Lastly, Figure 4.18 should get discussed. For loading higher than 2 MN elements that have entered the plastic region exist all over the depth. Thus the rectangles that describe the plastified region are excluded from the left part of the graph. However, the percentage of the plastified elements is available on the bottom right corner. It can be seen that for the highest two loading combinations this percentage is almost constant, which explains the approximately steady value on the right graph. The previous up and down of this stiffness should be connected with the redistribution of forces due to change of the number of the plastified elements.

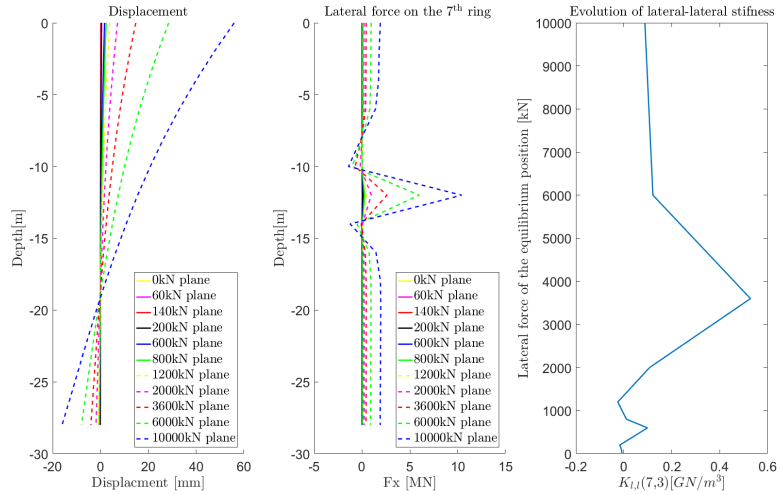

Figure 4.15: Behavior of $K^{l,l}(7,3)$ with increasing loading

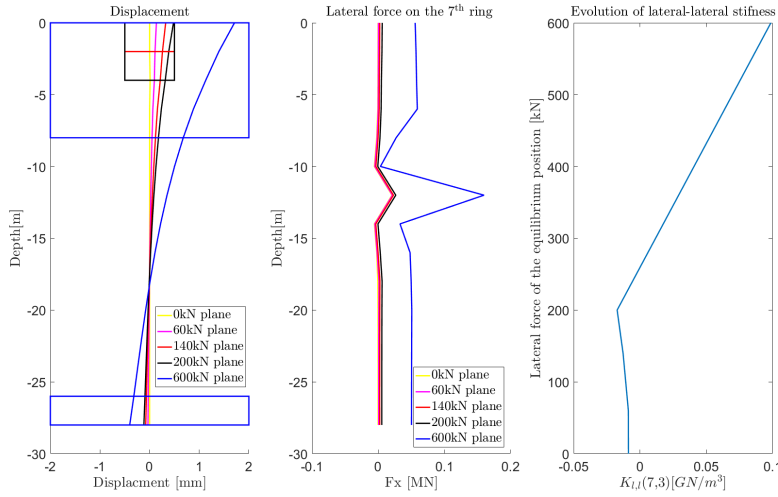

Figure 4.16: Behavior of $K^{l,l}(7,3)$ with increasing loading - small loading region

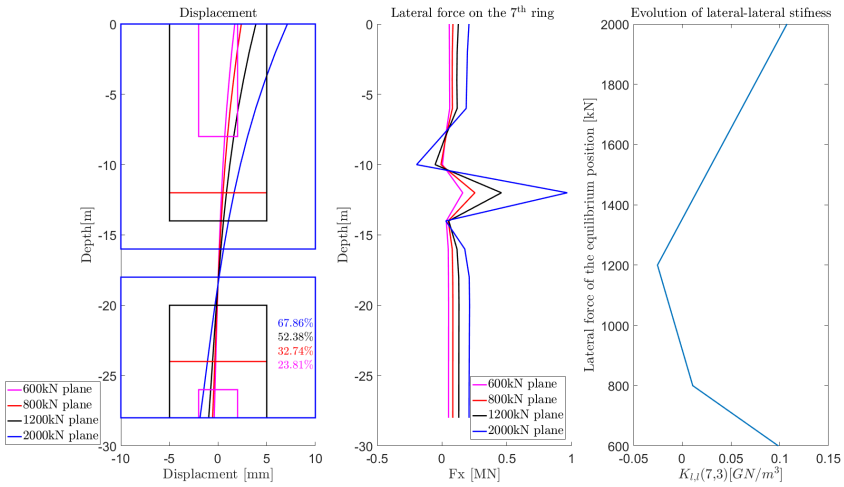

Figure 4.17: Behavior of $K^{l,l}(7,3)$ with increasing loading - intermediate loading region

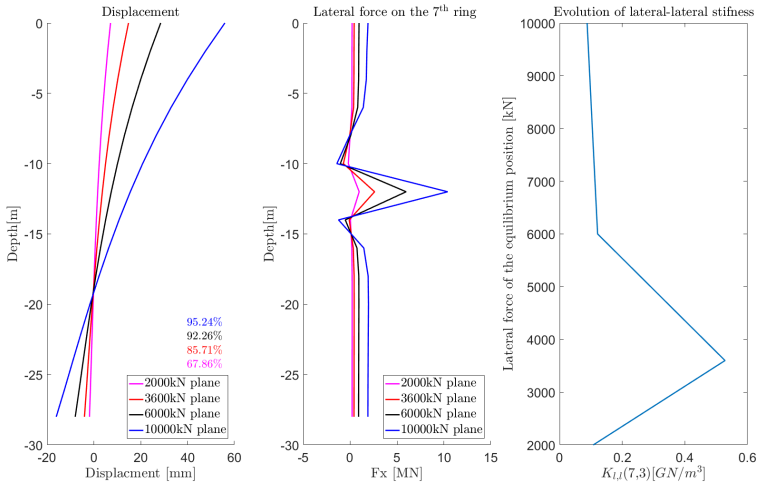

Figure 4.18: Behavior of $K^{l,l}(7,3)$ with increasing loading - high loading region

Concluding, a constant trend for the evolution (along the 3rd dimension) of the stiffness cells can not be found or predicted, therefore the interpolation difficulty is rising.

4.4.2. Interpolation technique

As it was explained on the previous paragraphs, a clear constant trend on the evolution of the single entities of the stiffness matrices can not be detected. Therefore, as it is illustrated on Figure 4.19 the interpolation based on polynomial functions can give erroneous results. The reason lies in the fact that when estimating with a polynomial function, it is silently assumed that the individual points at which the interpolation is established follow a specific distribution. Previously, it was shown that the evolution of each cell is very difficult to be put into boundaries, therefore such an interpolation is rational to fail.

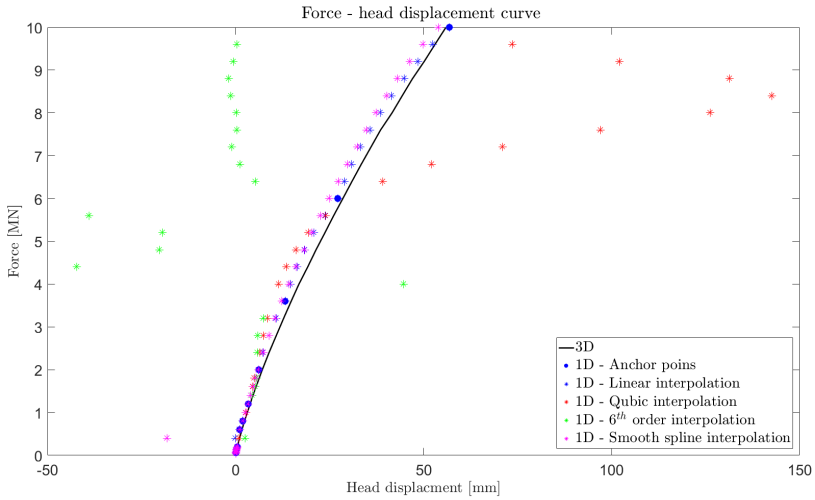

Figure 4.19: Force head displacement curve for different interpolation techniques - Case 1

On the other hand, this problem can be solved if the interpolation is constrained between two in a row planes every time. This can be achieved with either a linear or a spline interpolation technique. The term “smooth spline interpolation” mentioned on the Figure 4.19 is explained on Appendix B. On the aforementioned figure, the

linear interpolation gives very good result. However, Figure 4.20 represents the respective results of Case 2 . It is obvious that the interpolated solutions are far from being correct.

To improve the results of case 2, information before interpolating needs to be added. To clarify, more anchor points should be computed, meaning the stiffness matrices need to be calculated to extra equilibrium positions as well. By adding three extra planes on the matrices, at equilibrium positions of 5.6 MN, 7.2 MN and 8 MN the results improve significantly, see Figure 4.21. On this figure it can be seen that the smooth spline interpolation gives a good approximation, but the linear needs more anchor points. By increasing them even more, Figure 4.22 is produced. It can be seen that the linear interpolation gives a fair agreement with the 3D solution, but it is not smooth. The reason for this may be the extensive plastification zone, note that the head displacement touches 30 cm of deflection, in combination with the coarse discretization. On the other hand, by adding two extra anchor positions at case 1, at 4.8 MN and 8 MN, the results of linear interpolation can be improved and become smoother (Figure 4.23). Therefore, it can be concluded that the more equilibrium positions the better the approximation is.

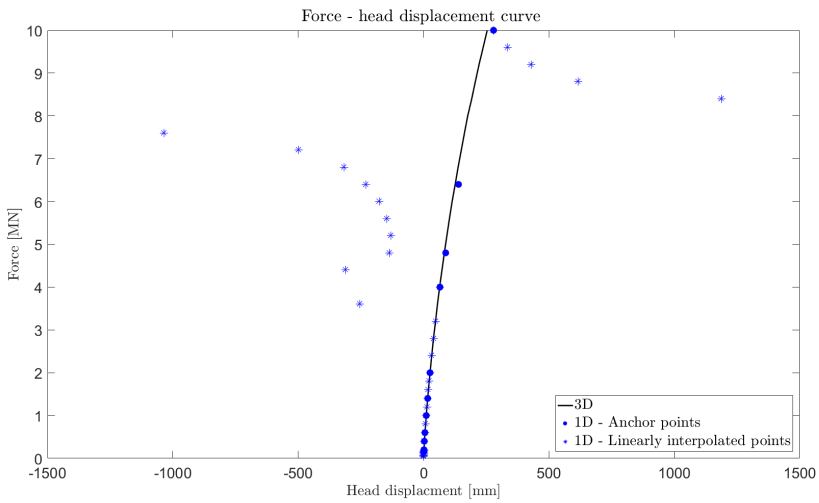

Figure 4.20: Force head displacement curve for case 2

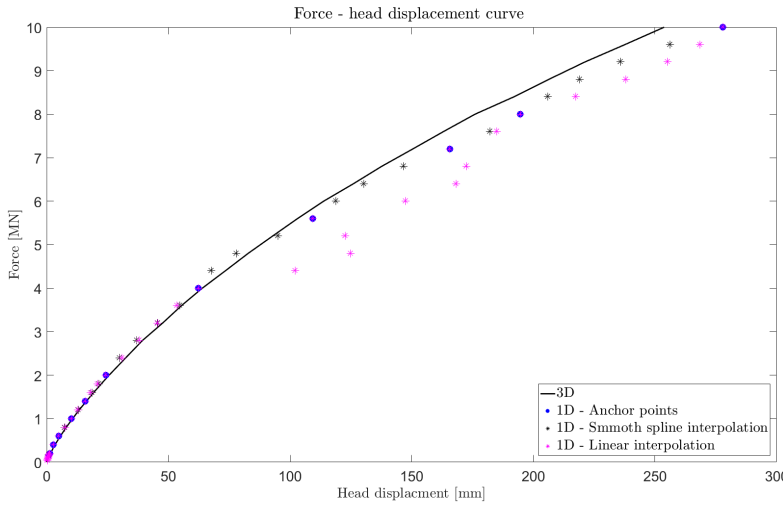

Figure 4.21: Force head displacement curve case 2 - Three extra equilibrium positions

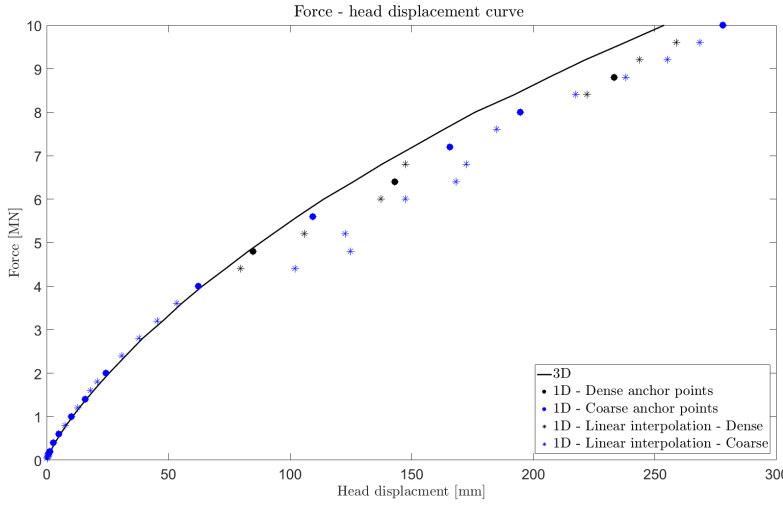

Figure 4.22: Force head displacement curve case 2 - Six extra equilibrium positions

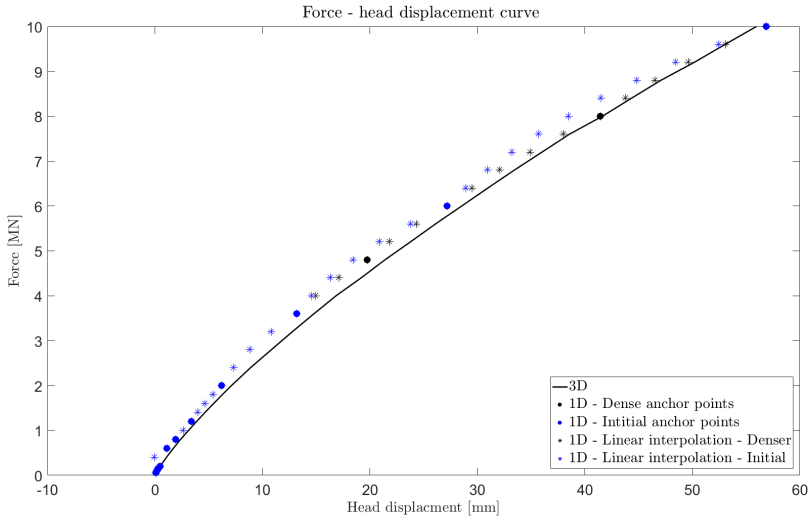

Figure 4.23: Force head displacement curve case 1 - Two extra equilibrium positions

4.5. Final Results

This section provides the final comparison of the 3D with the nonlinear nonlocal 1D effective model in terms of lateral force - head displacement (Figures 4.24 and 4.25) and overturning moment - head rotation curves, Figures 4.26 and 4.27. It can be seen that for both cases the final fit using linear interpolation is very well. It needs to be mentioned though that for the below results of case 1, two extra equilibrium positions are added as anchor points with respect to the initial selection. On the other hand, for case 2, six extra equilibrium positions were added compared to the initial estimation.

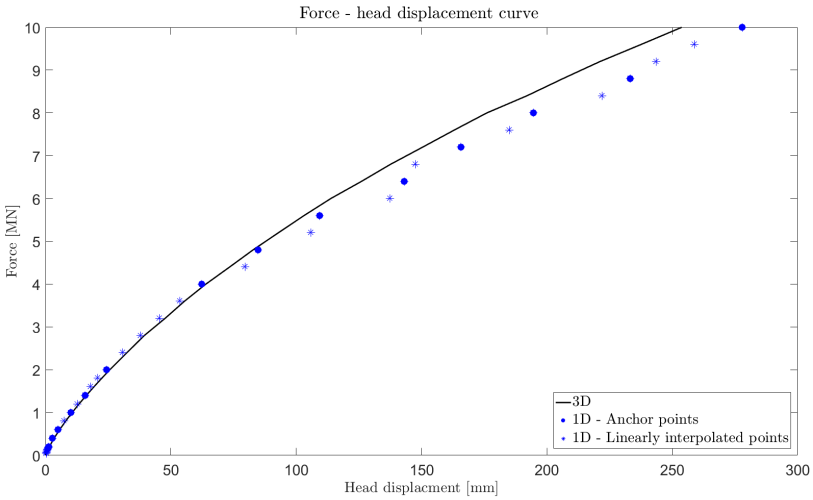

Figure 4.24: Force head displacement curve case 2

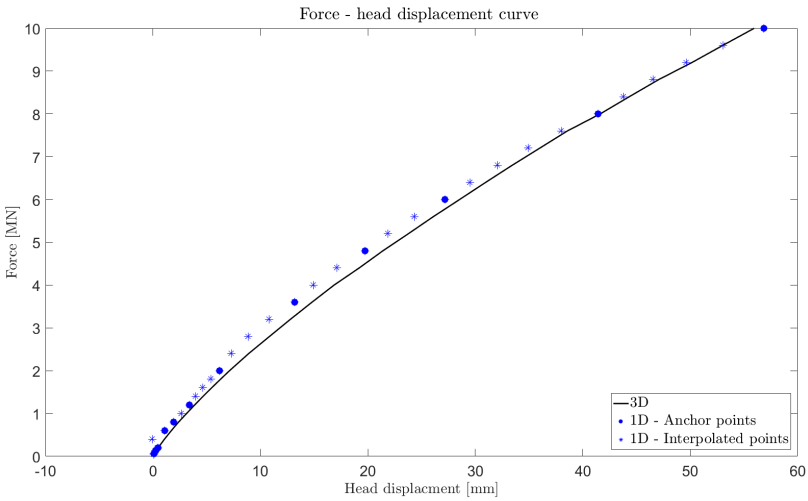

Figure 4.25: Force head displacement curve case 1

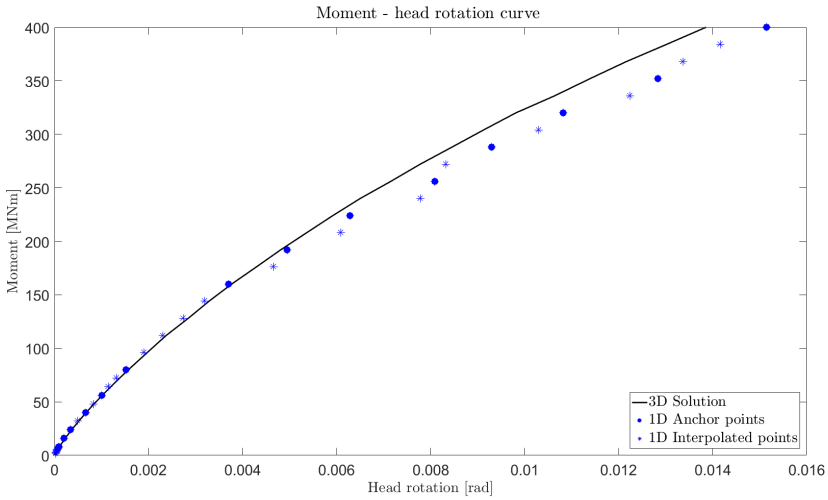

Figure 4.26: Moment head rotation curve case 2

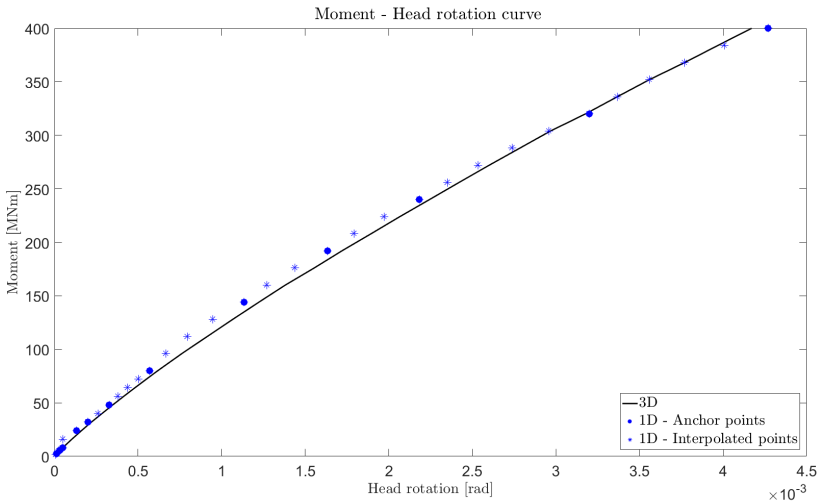

Figure 4.27: Moment head rotation curve case 1

5
Conclusions and Recommendations

A nonlocal 1D effective model able to predict the response of large monopiles in static and dynamic loading had recently been developed with the assumption of linear soil. This thesis project is an attempt to extend its applications to nonlinear continuum and static loading. The nonlinear nonlocal 1D effective model is a Timoshenko beam founded on a distributed, Winkler-type foundation, consisting of two types of fully coupled springs, lateral and rotational. It is established on results of 3D FEA. The stiffness matrices of the nonlinear nonlocal 1D effective model are expanded to a third dimension so as nonlinearity of the SSI is captured. The performance of the 1D effective model is assessed by comparing the lateral force - head displacement and the overturning moment - head rotation curves produced with the respective of 3D FEA. This chapter not only illustrates the conclusions of the study, but also gives recommendations for future work on the topic.

5.1. Conclusions

The project involved different challenges. For the reader's convenience and easiness, the conclusions follow the sequence of the outline of this study.

- Every plane on the 3rd dimension of the stiffness matrices represents the nonlocal (coupled) soil resistance at different equilibrium positions. The term equilibrium position refers to a state of displacement field. This is a deformed situation caused by loading the monopile at the mud-line level with a combination of a lateral force and an overturning moment. The selection of these positions is of great importance. If this choice is not fine enough, the interpolated results will be of low accuracy.

- To calculate each plane of the stiffness matrices, perturbations are imposed along the length of the pile. These should follow the direction of the deformed shape. At the beginning of the study, it was examined whether the results are influenced by the direction of the enforced perturbation. It was observed that they are sensitive and that imposing a unidirectional lateral perturbation along the depth is not appropriate for capturing the nonlocal soil response.
- The magnitude of the aforementioned perturbations is also very important. With smaller magnitude, better performance of the nonlinear nonlocal 1D effective model was observed.
- Even the smallest employed magnitude ($1 \cdot 10^{-5}\ m \backslash rad$ according to the type of perturbation) may induce extensive disturbance in the soil domain, especially at equilibrium positions of small load combination. Consequently, very large soil reactions are produced, which result in stiffer response of the nonlinear nonlocal 1D effective model than expected.
- The perturbations must be imposed in a 3D model excluding the stiffness of the pile. For this purpose, the displacement field of a 3D FEA was transfered to another 3D FE model as input. This transfer creates small discrepancies that in the end make the results less accurate. Moreover, the shape of the monopile was distorted. The preservation of the exact deformed shape of the MP proved to be important. In order to mitigate the induced error, a single 3D model approach was developed, producing the best results.
- The nonlinear nonlocal 1D effective model engages four stiffness matrices. The lateral-lateral represent lateral soil resistance due to pile lateral displacement, while the rotational-rotational symbolizes rotational soil resistance due to pile rotation. On the other hand, the last two, lateral-rotational and rotational-lateral, signify coupling of lateral resistance with rotation and vise versa. The main diagonal of the first two stiffness matrices are called “local” lateral and “local” rotational stiffness respectively. Counter-intuitively these terms increase when propagating along the 3rd dimension of the matrices. In contrast, the stiffness values exactly above and below the main diagonal of the implied matrices, are decreasing. The evolution of the remaining cells can be explained, but can not be predicted.
- A clear trend for the evolution of the planes of the stiffness matrices could not be identified. Therefore, single entity interpolation in between sequential planes was used. Both linear and spline interpolation was examined as interpolating techniques. Both give good results, but the spline interpolation give

slightly smoother results for the second case. However, the spline interpolation assumes a third order polynomial distribution, which is questionable, therefore it should not be chosen as "panacea" technique for alternative cases.

- Regarding the linear interpolation, it was found that the results become more accurate and the two curves (lateral force - head displacement and overturning moment - head rotation) get a better fit when the equilibrium positions have a finer selection. Even though, it was assumed and proved that in high loading the selection can be coarser, for the second case the initial selection was not adequate.

Concluding,the extension of the nonlocal 1D effective model to nonlinear SSI, under quasi-static loading, is considered successful. The majority of the individual comparisons (between the 3D and the 1D effective model solution along the length of the pile for a discrete load combination) showed excellent fitting, especially for high loading. The final aggregate performance in terms of lateral force - head displacement and overturning moment - head rotation curve is also very accurate.

Regarding the first case, the nonlinear nonlocal 1D effective model performs unexpectedly for an external force of 600 kN (Figure A.9). That is also the reason for the not very correct response at the interpolated 400 kN position (Figure 4.25). This behavior can be attributed to the fact that the rotation point for external loading of 600 kN is very close to a discretization depth. This means that the applied perturbation at this ring is relatively large compared to its equilibrium displacement (See also Appendix C). This "large disturbance" can be blamed for this unanticipated behavior. Generalizing, it could be the reason for the larger misfit observed in the small loading region compared to the misfit in the large loading region. A solution is offered in the next section.

5.2. Recommendations

This section is divided into three parts. Firstly, recommendations regarding extra validation of the exact procedure are given. Afterwards, suggestions concerning improvement of the method are made, while at the end a proposal for a slightly different methodology is presented.

First of all, recommendations for extra steps :

- A flexible pile behavior, according to Poulos [20], could be tested.
- It should be examined what the influence of finer meshing in the 3D FEA (consequently finer discretization of the 1D effective model) is on the accuracy of the nonlinear nonlocal 1D effective model.

- For the first case the examined force range could be extended. Even though the lateral force is high (10 MN), the head deflection of the pile is still relatively small.
- An in depth investigation of the redistribution of forces could be fruitful. When an element enters the plastic region, the surrounding elements react to any extra loading. An awareness of this redistribution's path would give an extra insight into the method.

Next, suggestions for improving the procedure :

- The soil modeling can be more realistic by adding layers of soil with different properties. The soil monopile interaction can be modeled more advanced. For example, contact elements that allow sliding and gaping can be used. Moreover, the area close to the pile can have reduced strength parameters to account for the skin friction in-between soil and pile elements.
- The magnitude of the imposed ring perturbation could be reduced even more, especially on cases it is applied on rings with small deflection at the equilibrium positions. In order to achieve this "small" kinematic loading, the uniformly, over depth, distributed magnitude of perturbation could vary. For instance, it could be a percentage of the deflection at each depth.
- A different selection process of the equilibrium positions can be followed. A more sophisticated procedure, for example amount of plastified elements on the domain, may prove to be more efficient and refinement of the equilibrium positions may be avoided.
- The nonlinear nonlocal 1D effective model should be extended to different overturning moment over lateral force ratio applications. A solution could be to expand the stiffness matrices in a 4^{th} dimension to capture the dependence of the response to this ratio. Every shelf (4^{th} dimension) will consist of 3D matrices calculated as described in this study, but for different moment over force ratio.
- The developed nonlinear nonlocal 1D effective model engages secant stiffness matrices. If an extension to cyclic loading is desired, a transformation to a model employing tangent stiffness matrices is required.

Finally, a possibly beneficial slight adjustment of the method is discussed. The imposed lateral perturbations refer to nodes. However, this perturbation introduces

intense shear on the horizontal plane for the attached soil elements. In contrast, we are interested on lateral soil resistance, which can be connected to surface movement rather than disturbance on a line. Therefore, the proposal is to perform perturbations of areas of the circumference and not of nodes when calculating the lateral-lateral and rotational-lateral stiffness matrix. The remaining process can remain unchanged. Of course, this alteration should firstly be checked on soil with linear properties to prove its validity.

To summarize the research, the nonlinear nonlocal 1D effective model is able to accurately predict the response of a monopile foundation under quasi-static loading, the complete process to be followed is illustrated in Appendix D. However, its applicability was examined at a specific ratio of overturning moment over lateral force. Therefore, the model should get extended so as it predicts the response to different quasi-static load combinations as well. When it proves its validity, an attempt to broaden its application range to dynamic loading should be made. Upon this accomplishment, it can be used in the offshore wind industry so as advanced nonlinear SSI is incorporated in the design of monopile foundations.

A

Comparison of equilibrium positions

A.1. Case 1

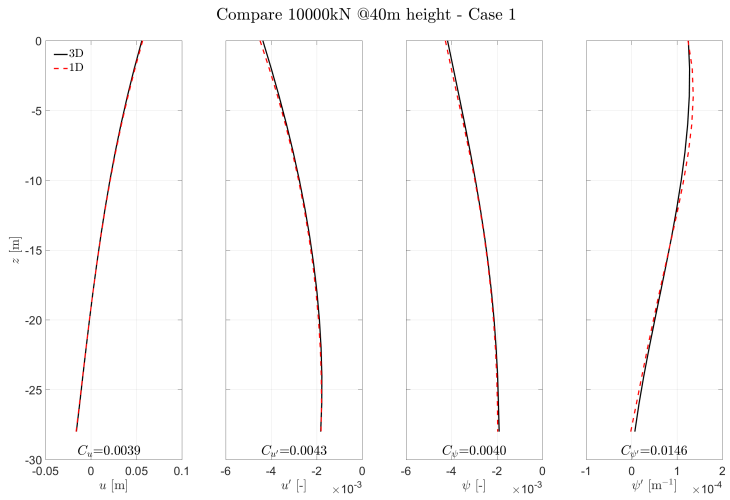

Figure A.1: Comparison of effective 1D model with 3D

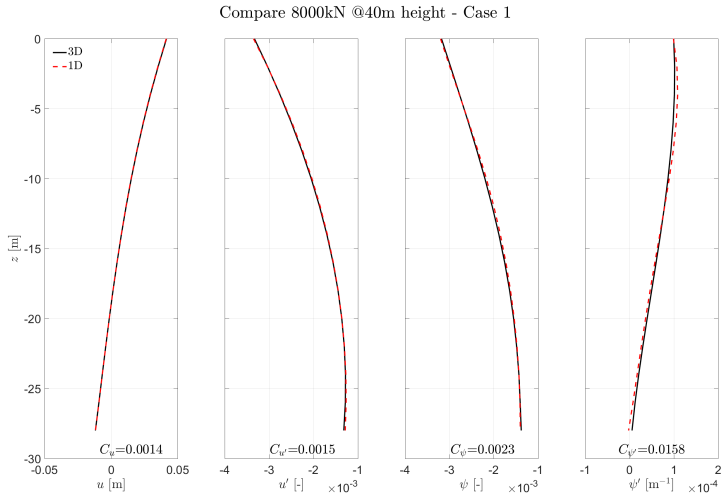

Figure A.2: Comparison of effective 1D model with 3D

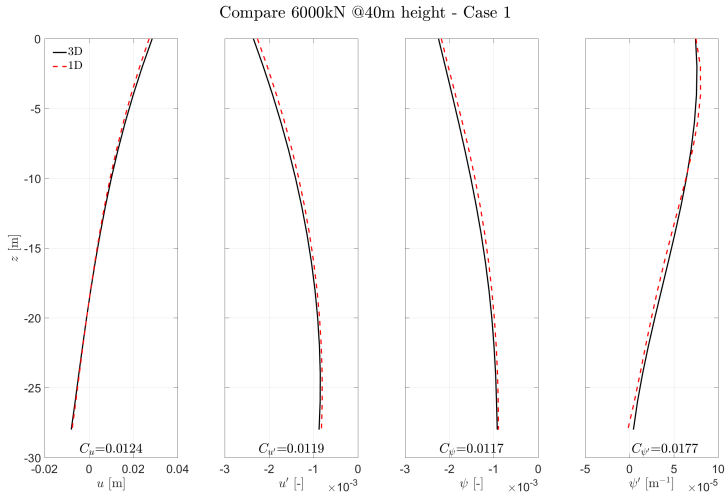

Figure A.3: Comparison of effective 1D model with 3D

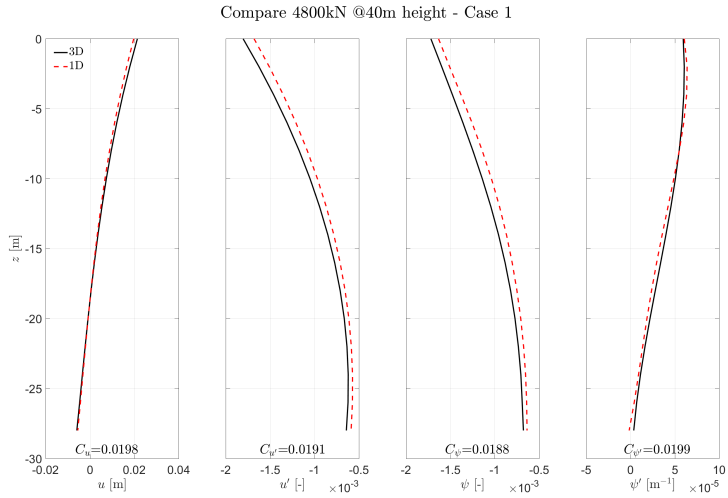

Figure A.4: Comparison of effective 1D model with 3D

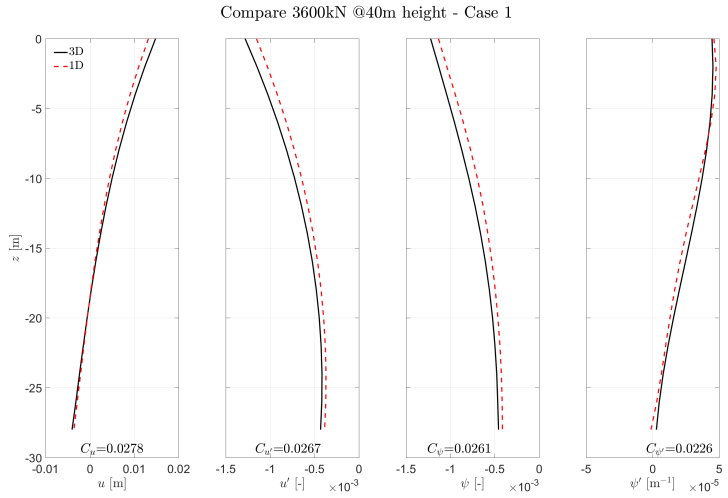

Figure A.5: Comparison of effective 1D model with 3D

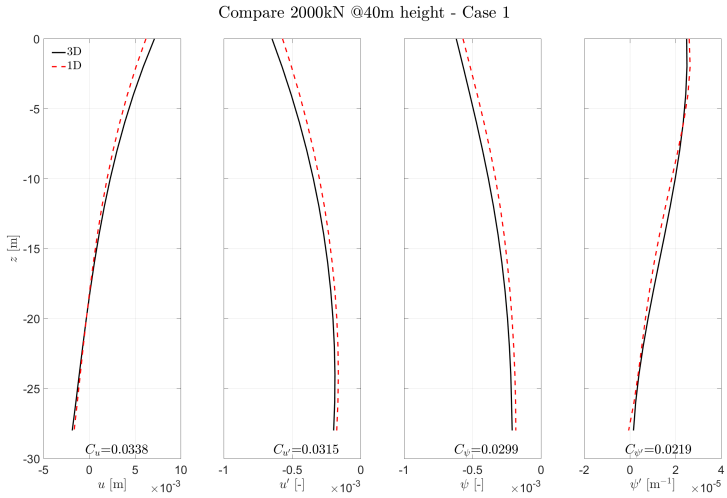

Figure A.6: Comparison of effective 1D model with 3D

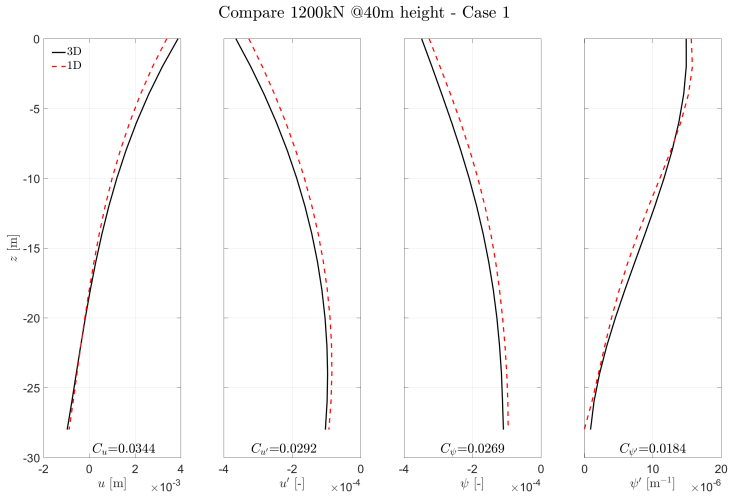

Figure A.7: Comparison of effective 1D model with 3D

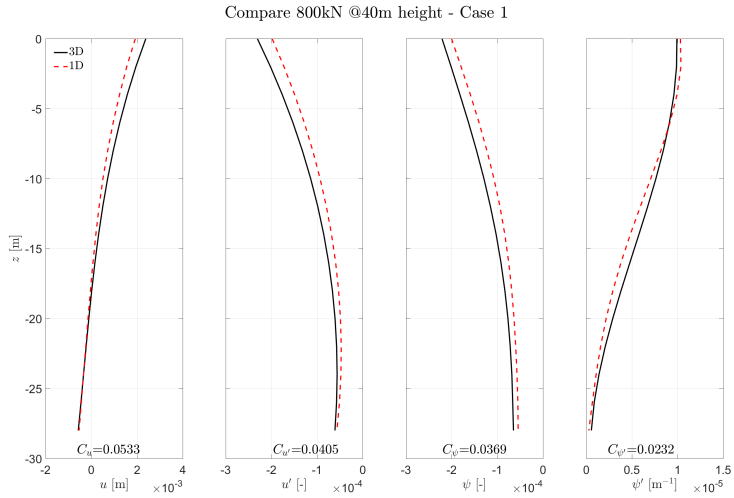

Figure A.8: Comparison of effective 1D model with 3D

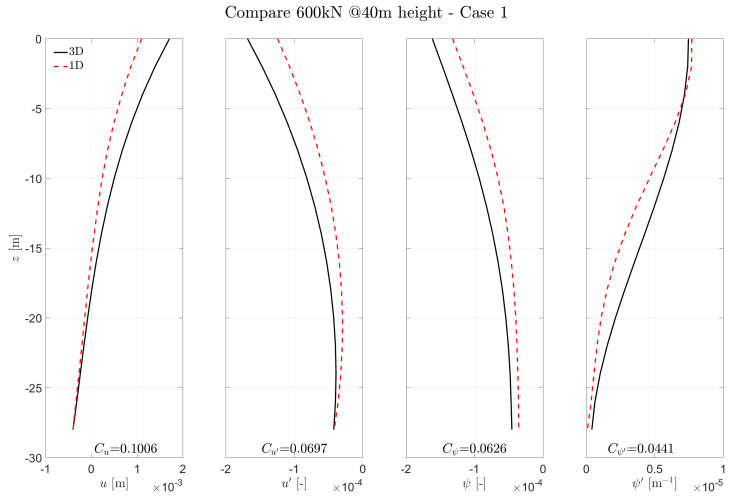

Figure A.9: Comparison of effective 1D model with 3D

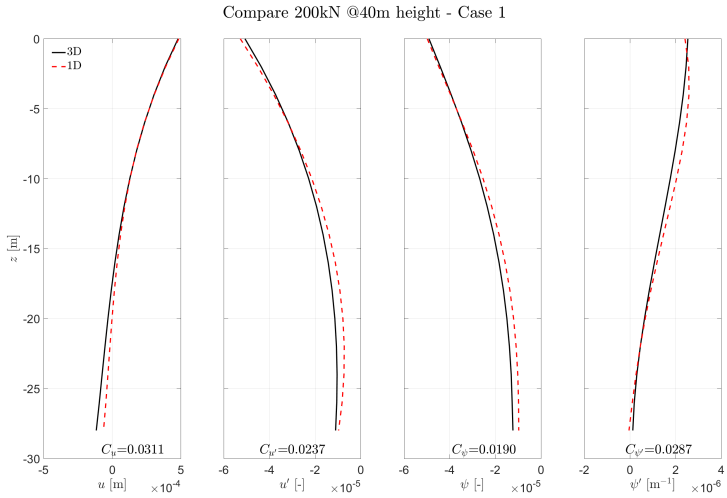

Figure A.10: Comparison of effective 1D model with 3D

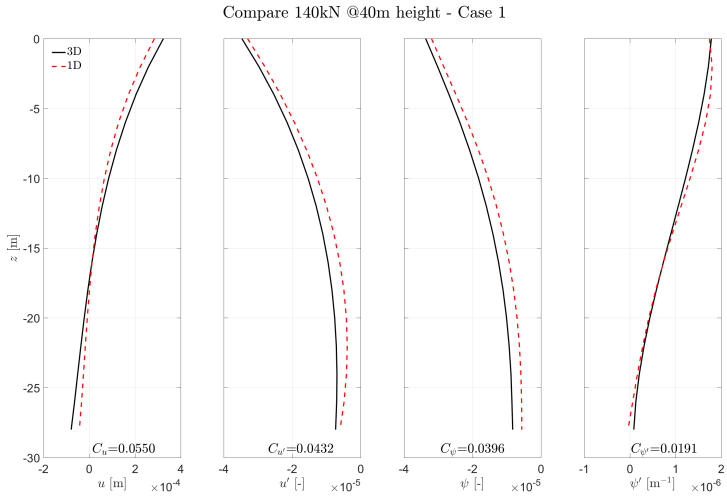

Figure A.11: Comparison of effective 1D model with 3D

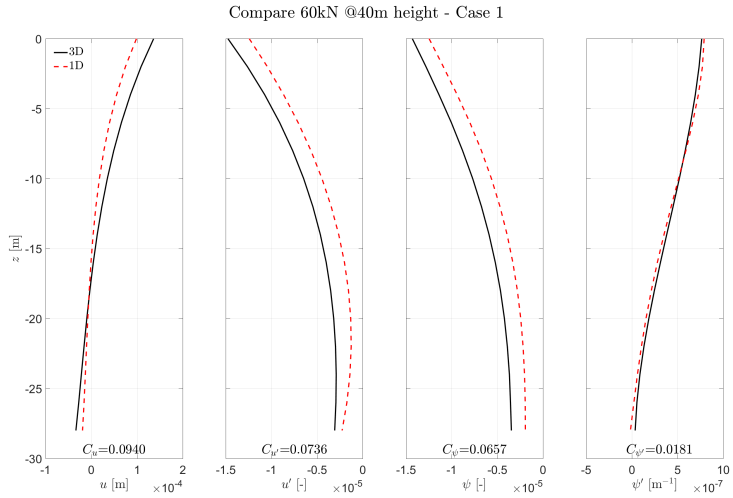

Figure A.12: Comparison of effective 1D model with 3D

A.2. Case 2

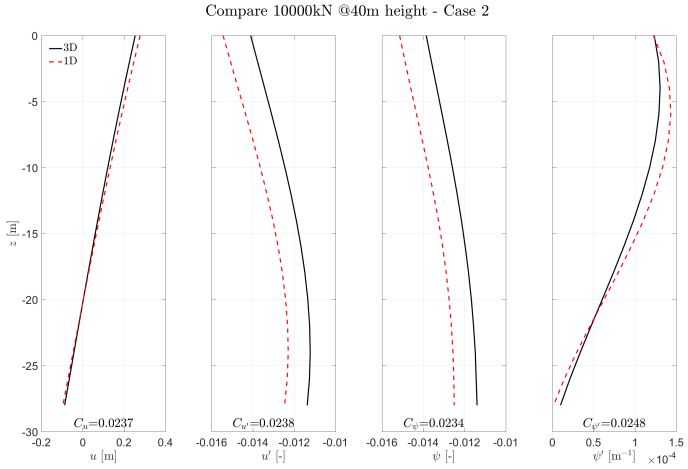

Figure A.13: Comparison of effective 1D model with 3D

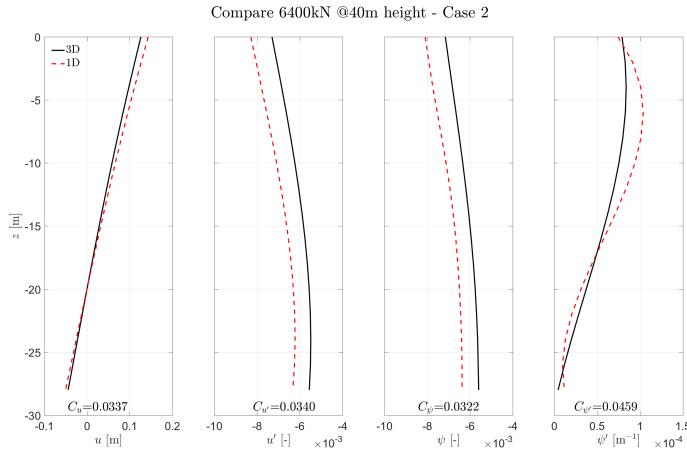

Figure A.14: Comparison of effective 1D model with 3D

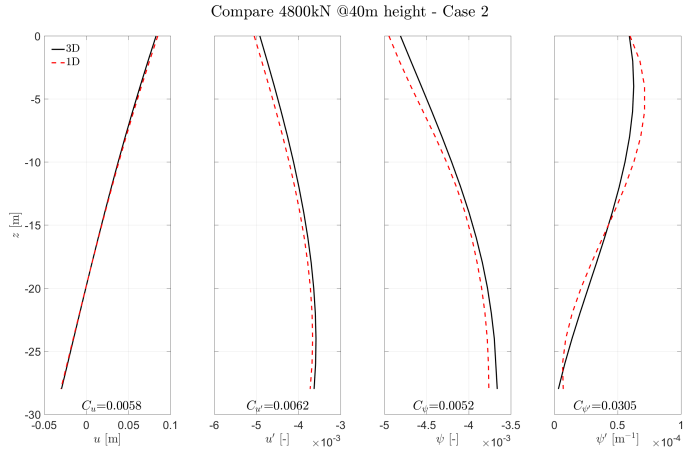

Figure A.15: Comparison of effective 1D model with 3D

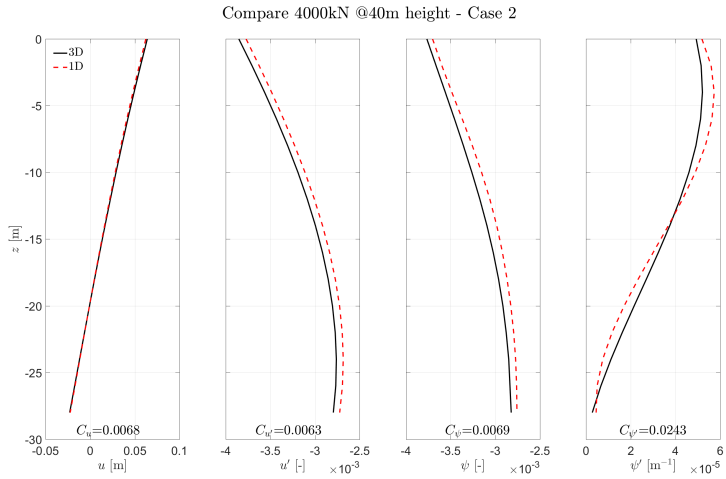

Figure A.16: Comparison of effective 1D model with 3D

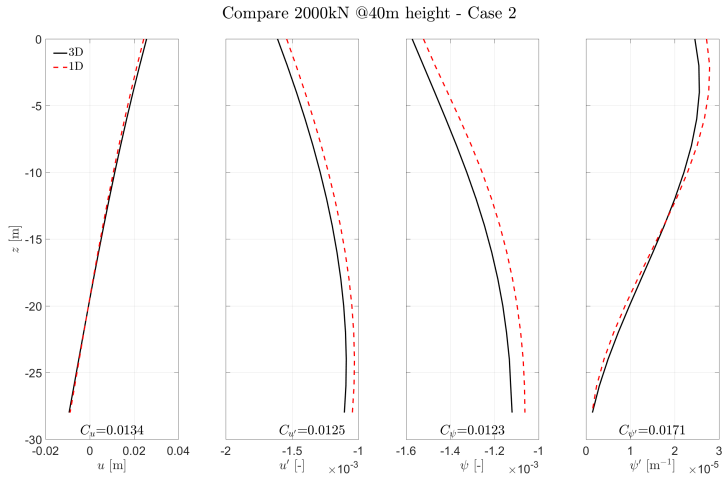

Figure A.17: Comparison of effective 1D model with 3D

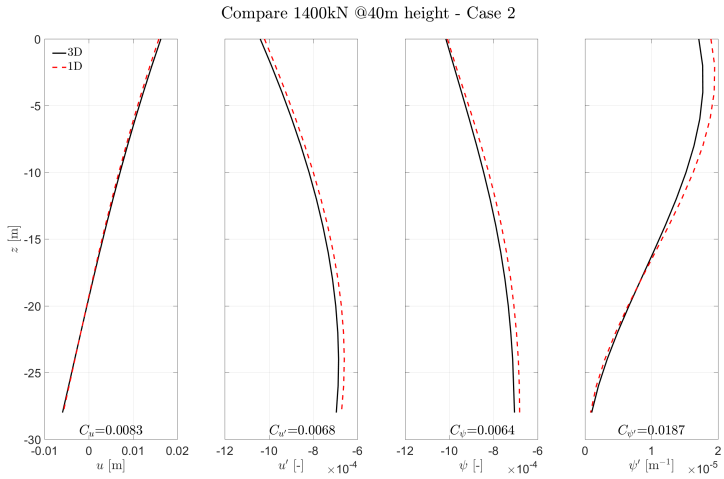

Figure A.18: Comparison of effective 1D model with 3D

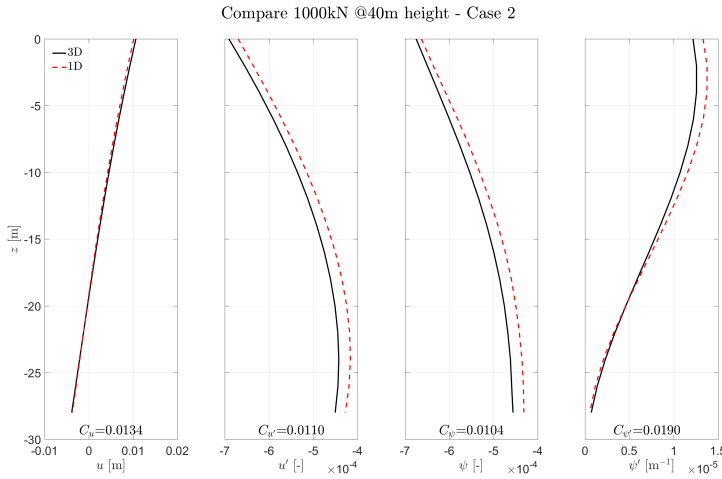

Figure A.19: Comparison of effective 1D model with 3D

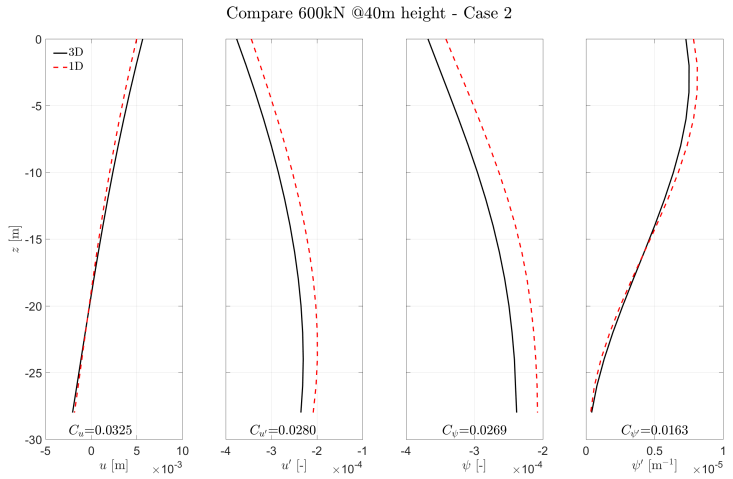

Figure A.20: Comparison of effective 1D model with 3D

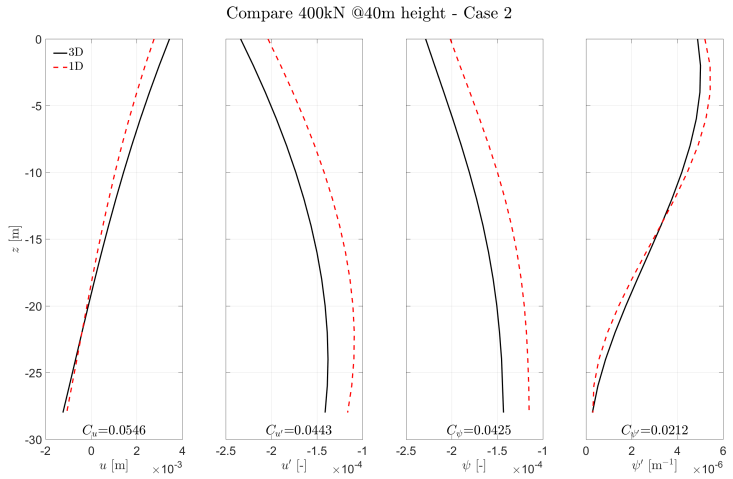

Figure A.21: Comparison of effective 1D model with 3D

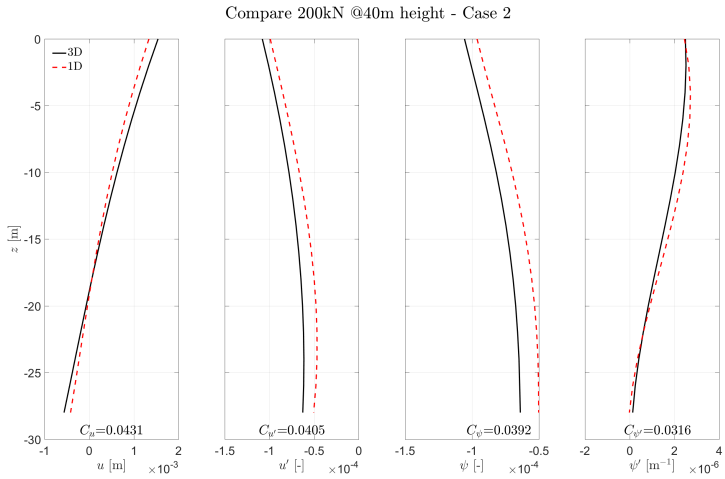

Figure A.22: Comparison of effective 1D model with 3D

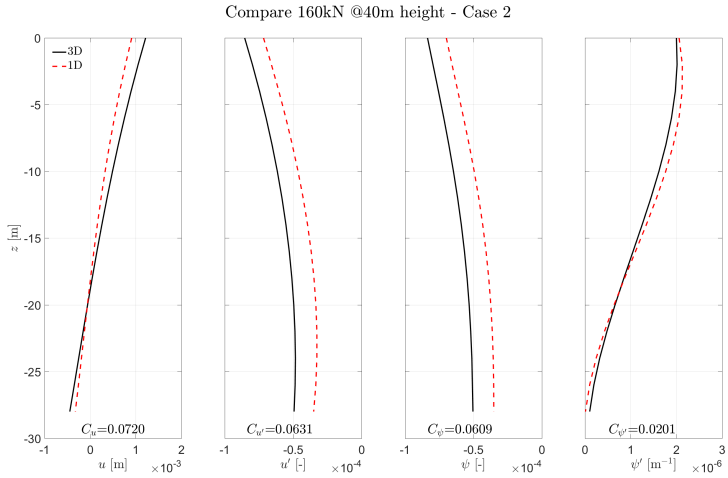

Figure A.23: Comparison of effective 1D model with 3D

B

Smooth spline interpolation

Spline is an interpolation based on piecewise polynomial fitting [28]. To clarify, in-between every two anchor points a polynomial function describes the distribution of under examination parameter. The order of the polynomial fitting used in this study was third. Therefore, there are 4 unknowns for every fitting function.

According to the number of anchor points, the total number of unknowns changes. For example, for case 1, employing 11 equilibrium positions, 40 unknowns for each cell of all the stiffness matrices should be computed. Thus, equal number of equations is needed. The mathematical expression of a spline and the equations for calculating the terms of the cubic spline are available on the following equations:

$$S(x) = \begin{cases} C_1(x), x_0 \leq x \leq x_1 \\ \cdots \\ C_i(x), x_{i-1} \leq x \leq x_i \\ \cdots \\ C_{10}(x), x_9 \leq x \leq x_{10} \end{cases}$$

$$\begin{gathered} C_i(x_{i-1}) = y_{i-1} \\ C_i(x_i) = y_i \\ C_i'(x_i) = C_{i+1}'(x_i) \\ C_i''(x_i) = C_{i+1}''(x_i) \\ C_1''(x_0) = 0 \\ C_{10}''(x_{10}) = 0 \end{gathered} \tag{B.1}$$

However, in this study a “smooth” spline interpolation was engaged, using Matlab. The term smooth comes from the fact that the spline is combined with a least square approximation, meaning there is a smoothing parameter that introduces a combination of least square and spline interpolation [16]. This parameter was not specified, but Matlab was automatically computing the best fit.

C

Unexpected behavior of 1D effective model

The behavior of the nonlinear nonlocal 1D effective model in case 1 for the equilibrium position of 600 kN is unanticipated (Figure A.9). The left part of Figure C.1 shows the deformed shape for this equilibrium position. Moreover, the deflection at -18 m is mentioned on the plot. It can be seen that it is smaller than the applied perturbation ($0.01mm$), which opposes to the idea of imposing small lateral disturbances. This relatively large magnitude of perturbation is considered to be the reason for the unpredictable large misfit (Figure A.9).

The calculated stiffness matrices at the aforementioned equilibrium position also influence the performance of the nonlinear nonlocal effective 1D model for similar loading, because they are used as anchor planes for the interpolation. That was the case for external lateral force of 400 kN (see Figure 4.25). To overcome this problem, it was decided to derive the stiffness matrices of the 400 kN equilibrium position following the perturbation procedure. However, the quality of the fit between the 1D and the 3D results is low (Figure C.2). A suspected reason is again the relative magnitude of perturbation. As illustrated on the right subplot of Figure C.1, the deflection at - 18 m is almost 100 times smaller than the imposed perturbation on this level.

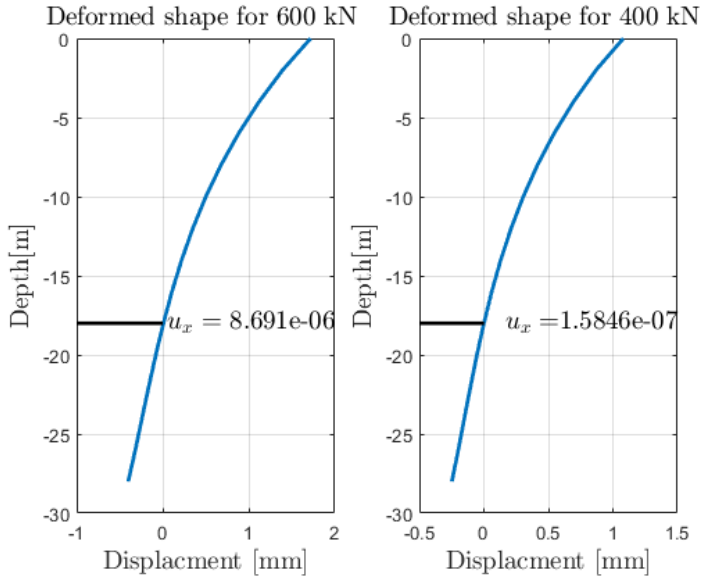

Figure C.1: Deformed shape for equilibrium positions at 600 kN and 400 kN

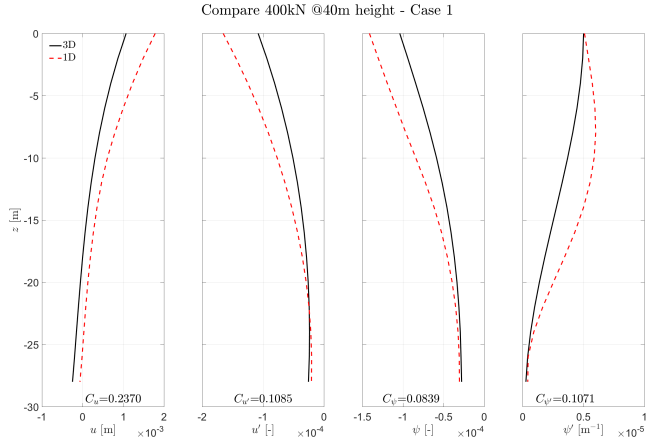

Figure C.2: Comparison of effective 1D model with 3D

D

Procedure

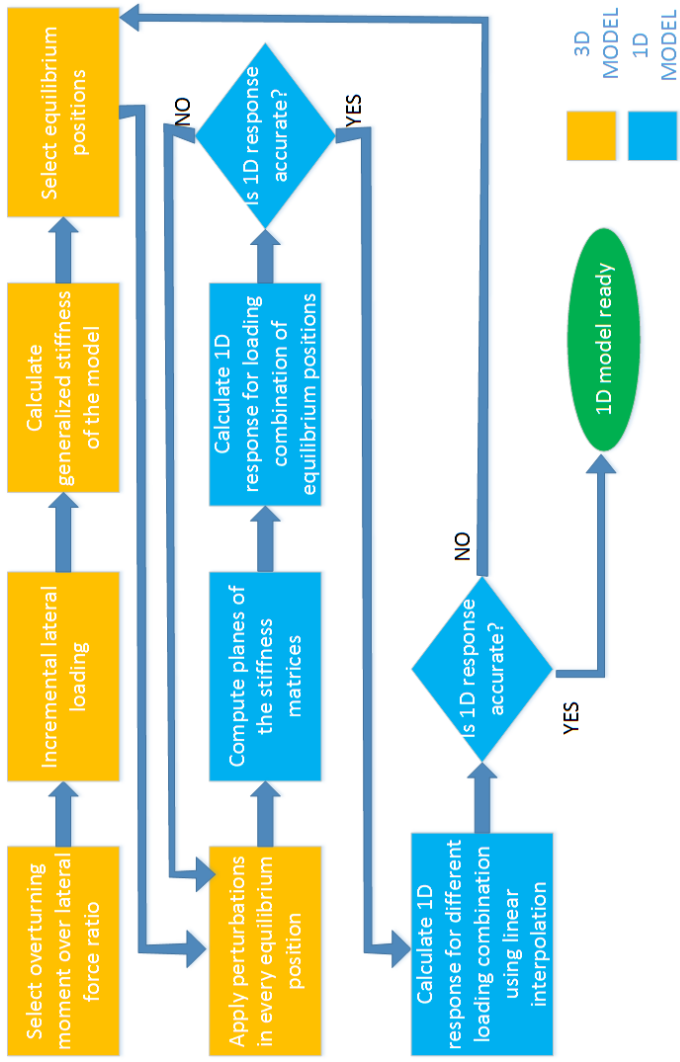

Figure D.1: Flowchart of the procedure for building the nonlinear nonlocal 1D effective model

Bibliography

[1] K Abdel-Rahman and M Achmus. Finite element modelling of horizontally loaded monopile foundations for offshore wind energy converters in germany. In *Proceedings of the International Symposium on Frontiers in Off-shore Geotechnics (ISFOG). Edited by S. Gourvenec and M. Cassidy. Taylor and Francis, Perth*, pages 391–396, 2005.

[2] ANSYS Mechanical APDL. Element reference. *ANSYS Release 18.2*, 2017.

[3] ANSYS Mechanical APDL. Material reference. *ANSYS Release 18.2*, 2017.

[4] JH Atkinson. Experimental determination of stress-strain-time characteristics in laboratory and-in-situ tests. general report. In *Proc. 10th Eur. Conf. Soil Mech. and Fnd Engng*, volume 3, pages 915–956, 1991.

[5] KT Brødbæk, M Møller, SPH Sørensen, and Anders Hust Augustesen. Review of py relationships in cohesionless soil. 2009.

[6] BW Byrne, R McAdam, HJ Burd, G Houlsby, C Martin, L Zdravković, DMG Taborda, DM Potts, RJ Jardine, M Sideri, et al. New design methods for large diameter piles under lateral loading for offshore wind applications. In *3rd International Symposium on Frontiers in Offshore Geotechnics (ISFOG 2015), Oslo, Norway, June*, pages 10–12, 2015.

[7] BW Byrne, RA McAdam, H Burd, GT Houlsby, CM Martin, WJAP Beuckelaers, L Zdravkovic, DMG Taborda, DM Potts, RJ Jardine, et al. Pisa: new design methods for offshore wind turbine monopiles. 2017.

[8] John Conti, Paul Holtberg, Jim Diefenderfer, Angelina LaRose, James T. Turnure, and Lynn Westfall. International energy outlook 2016 with projections to 2040.

[9] World Energy Council. World energy resources. Technical report, 2016.

[10] GL DNV. Support structures for wind turbines. *Standard DNV GL-ST-0126*, 2016.

[11] AG Drachmann. Heron's windmill. *Centaurus*, 7(2):145–151, 1961.

[12] Nikos Gerolymos and George Gazetas. Development of winkler model for static and dynamic response of caisson foundations with soil and interface nonlinearities. *Soil Dynamics and Earthquake Engineering*, 26(5):363–376, 2006.

[13] Ignatius Po Lam and Geoffrey R Martin. Seismic design for highway bridge foundations. In *Lifeline Earthquake Engineering: Performance, Design and Construction*, pages 7–21. ASCE, 1986.

[14] K Lesny and J Wiemann. Design aspects of monopiles in german offshore wind farms. In *Proceedings of the International Symposium on Frontiers in Offshore Geotechnics*, pages 383–389. AA Balkema Publishing, 2005.

[15] Adam Lichtl and Stephen Jones. Full scale simulation of spacex's mars rocket engine. 16:00-21:00 min, 2015.

[16] MATLAB. *version R2017a*. The MathWorks Inc., Natick, Massachusetts, 2017.

[17] Hudson Matlock. Correlations for design of laterally loaded piles in soft clay. *Offshore Technology in Civil Engineering Hall of Fame Papers from the Early Years*, pages 77–94, 1970.

[18] Michael W O'Neill and Jack M Murchison. *An evaluation of py relationships in sands*. University of Houston, 1983.

[19] TKI Wind op Zee. Cost reduction options for offshore wind in the netherlands fid 2010-2020, 2015.

[20] Harry G Poulos and Tim S Hull. The role of analytical geomechanics in foundation engineering. In *Foundation engineering: Current principles and practices*, pages 1578–1606. ASCE, 1989.

[21] Trevor J Price. James blythbritain's first modern wind power pioneer. *Wind engineering*, 29(3):191–200, 2005.

[22] Lymon C Reese, William R Cox, and Francis D Koop. Analysis of laterally loaded piles in sand. *Offshore Technology in Civil Engineering Hall of Fame Papers from the Early Years*, pages 95–105, 1974.

[23] Søren Peder Hyldal Sørensen, Lars Bo Ibsen, and Anders Hust Augustesen. Effects of diameter on initial stiffness of py curves for large-diameter piles in sand. In *The European Conference on Numerical Methods in Geotechnical Engineering*, pages 907–912. CRC Press LLC, 2010.

[24] Karl Terzaghi. *Theoretical soil mechanics*. Chapman And Hall, Limited.; London, 1951.

[25] Karl Terzaghi, Ralph B Peck, and Gholamreza Mesri. *Soil mechanics in engineering practice*. John Wiley & Sons, 1996.

[26] WG Versteijlen, JM de Oliveira Barbosa, KN van Dalen, and AV Metrikine. Dynamic soil stiffness for foundation piles: Capturing 3d continuum effects in an effective, non-local 1d model. *International Journal of Solids and Structures*, 134:272–282, 2018.

[27] WG Versteijlen, AV Metrikine, and KN van Dalen. A method for identification of an effective winkler foundation for large-diameter offshore wind turbine support structures based on in-situ measured small-strain soil response and 3d modelling. *Engineering Structures*, 124:221–236, 2016.

[28] Wikipedia contributors. Spline interpolation — Wikipedia, the free encyclopedia, 2018. [Online; accessed 01-August-2018].

[29] Wikipedia contributors. Superposition principle — Wikipedia, the free encyclopedia, 2018. [Online; accessed 16-August-2018].

TU Delft Delft University of Technology

SIEMENS Gamesa RENEWABLE ENERGY